Original research article

Institution of MECHANICAL ENGINEERS

Journal of AEROSPACE ENGINEERING

Proc IMechE Part G:
J Aerospace Engineering
2026, Vol. 0(0) 1–25

DOI: 10.1177/09544100261447562
journals.sagepub.com/home/pig
Sage

Modeling and experimental research on zero-bias thermal stability of the torque motor for aviation electro-hydraulic servo valves

Leilei Niu[1], Shenghong Ge[1,2], Zhichuang Chen[3], Haijun Zhu[2] and Yuchuan Zhu[1]

Abstract

A permanent magnet torque motor's (PMTM) zero is very easily shifted under the dual thermal changes of structure and material in a high-temperature service environment. The aero-engine electro-hydraulic servo valve's service performance is greatly impacted by the thermal stability of zero bias. However, it is difficult for designers to maintain the stability of the servo valves' zero position since the fundamental reasons of zero-bias and its effective suppression measures are still unclear. Aiming at this issue, the mechanism of the generation and evolution of the zero-bias of PMTM is analyzed deeply, and a zero-bias predictive model of PMTM is created by combining response surface methods and finite element analysis in this paper. Relative experiments are conducted, and the findings reveal that the practical and theoretical values of the zero-bias distribution characteristic parameters for batch PMTMs are all of the same order of magnitude. The greatest relative errors between theoretical and actual values for the output displacement of the feedback rod ball of PMTM at 30°C and 180°C are 10.6% and 10.7%, respectively. Additionally, the armature assemblies' thermo-solid coupling deformation has the biggest impact on the thermal drift of zero-bias for PMTM at high temperature. The zero-bias of PMTM at room temperature can be efficiently suppressed by preferentially limiting the range of vertical difference between the four air gaps. In conclusion, this work offers a useful theoretical reference for studying the zero-bias of electro-hydraulic servo valves.

Keywords

electro-hydraulic servo valves, torque motor, zero-bias, predictive model, high-temperature experiment

Received: 3 November 2025; accepted: 13 April 2026

Introduction

The electro-hydraulic control valve, as the core control element in the aviation hydraulic transmission system, is designed to efficiently and accurately convert the input low-power electrical signal (current or voltage) into hydraulic power output (flow and pressure), thereby controlling the motion direction or speed of the actuator. Whether the electro-hydraulic servo valve[1] seeks ultimate dynamic accuracy or the electro-hydraulic directional valve[2] ensures dependable commutation, the essential aim is to complete the energy form conversion of 'electric-mechanical-hydraulic.' The servo valve, a precise electromagnetic-mechanical-hydraulic integrated component with a more sophisticated structure and high integration of multi-physical fields, is widely employed in the field of accurate and dependable braking and brake control of equipment in various industries, including aerospace. Examples include vector deflection control,[3,4] guide vane angle adjustment,[5] fuel flow control,[6,7] and so on.

However, because the electro-hydraulic servo valve frequently operates close to the zero position, a variety of factors, including processing error of magnet pole face, interference and screw connection, electromagnetic deflection of the armature, thermal-solid coupling deformation of the structure, and magnetic performance degradation, can easily cause the four air gaps of PMTM to deviate from their ideal design value. The addition of a temperature field, in particular, will exacerbate the problem. Early in the product design process, effective material selection and fit clearance design have a substantial buffering influence on the thermal stress distribution between precision parts during the high-temperature

[1]College of Mechanical & Electrical Engineering, Nanjing University of Aeronautics and Astronautics, Nanjing, China
[2]AVIC Nanjing Servo Control System Co., Ltd, Nanjing, China
[3]AECC Aero Engine Control System Institute, Wuxi, China

Corresponding author:
Yuchuan Zhu, College of Mechanical & Electrical Engineering, Nanjing University of Aeronautics and Astronautics, 29 Yudao Street, Nanjing, Jiangsu Province 210016, China.
Email: meeyczhu@nuaa.edu.cn

process.[8] Temperature affects PMTM material parameters such as the elastic element's Young's modulus and Poisson's ratio, as well as the thermal degradation of magnetic properties; structural parameters include the thermo-solid coupling deformation of the magnetic circuit and armature components. As a result, the zero position of PMTM is prone to drift due to the multiple coupling heat effects of the aforementioned manufacturing, assembly, structure, material, and temperature, resulting in the stability and reliability of the zero bias performance of the electro-hydraulic servo valve lagging significantly behind the development needs of the equipped main engine. Furthermore, since the aviation manufacturing business has grown, a multi-variety and batch production mode has steadily emerged as the primary mode of production.[9] The basic premise of quality performance prediction is to create a quality prediction model that takes key influencing aspects of the manufacturing process as input and outputs a quality characteristic index. Mass-produced servo valves, in particular, have poor zero-bias performance consistency at high-temperature service conditions, and there are gaps and shortcomings in the internal mechanism and suppression technology. It is critical to do predictive modeling studies on the zero-bias and performance consistency of mass-produced servo valves.

The zero-bias performance of the PMTM, which is the primary motor conversion component of the electro-hydraulic servo valve, has a significant impact on the servo valve's zero-bias stability. Its output properties have been extensively examined during the last few decades. Merritt[10] created a rudimentary magnetic circuit model of PMTM in the 1960s. Subsequent researchers enhanced this model by including additional features such as permanent magnet reluctance and flux leakage,[11] magnetic element reluctance,[12] coil flux leakage,[13] fringing effect,[14] eddy current,[15] and unequal air-gap thickness.[16] Chen et al.[17] developed an improved model that can account for a variety of parameters, such as non-working air gaps, the fringing effect at limiting holes, the nonlinear permeability of soft magnetic material, and so on. The significance of each element on the created model's accuracy was then quantitatively evaluated. The ambient temperature of an electro-hydraulic servo valve used in aero engines varies greatly. The temperature of the fuel metering device of an aviation engine can range from −40°C to 120°C.[18] Yan et al.,[19] Kang et al.,[20] Ma et al.,[21] and Liu et al[22] examined the thermal impacts on EHSV performance and developed a temperature-dependent model for PMTM. The models described above are all simplified analytical models based on a single PMTM. There are few studies on the PMTM zero-bias model, and essentially no research that takes all of the above aspects into account when predicting the zero-bias characteristics of PMTM or servo valves. The existing study on the factors of zero-bias instability of the servo valve can be described as screw assembly stress,[23] air gap length,[20,24] structure thermal deformation,[25] and magnetic parameter temperature change.[21] Furthermore, the majority of them concentrate on the impact of single functional component structure manufacturing parameters and single physical field performance parameter changes on the zero-bias performance of the servo valve, which fails to reveal the zero-bias generation mechanism and evolution of the servo valve under the combined action of multi-factor and multi-physical field coupling. Furthermore, there is a scarcity of relevant theoretical references and technical support for the issue of poor zero-bias consistency encountered by mass-produced servo valves.

In this paper, the torque motor of a specific type of electro-hydraulic servo valve is used as the research object, and a prediction model of the zero-bias of PMTM of the electro-hydraulic servo valve is proposed, incorporating response surface methodology and finite element analysis. The model takes into account a variety of parameters, such as machining errors on magnetic pole surfaces, interference and screw connections, armature electromagnetic deflection, and temperature impacts on structural deformation and magnetic characteristics. To validate the model, tests are performed on the zero-bias of batch PMTMs at room temperature, as well as the output displacement of a single PMTM at high temperature. The validated model is used to analyze the effect of various parameters on the zero-bias of PMTM, and process methods are given to suppress the zero-bias of PMTM at room temperature.

Surrogate model of static output displacement for PMTM

Structure of PMTM and physical model of electromagnetic torque

The structure of the investigated PMTM, depicted in Figure 1(a), consists of setscrews, a support tube, an armature, adjusting shims, support blocks, an upper yoke, permanent magnets, control coils, a bourdon tube, a lower yoke, and a fixed base. As shown in Figure 1(b), the working principle of this PMTM has been described in depth in our earlier work,[17] thus no additional explanation is required here.

An equivalent magnetic circuit model for the PMTM is shown in Figure 2, which builds upon the equivalent magnetic circuit physical model of the PMTM given in Ref. 17. The resistance of the upper and lower yokes, the fringing effects at the limiting holes, and eddy current effects within the magnetic components are all excluded from the model. Our earlier work[17] demonstrated that these parameters have no effect on the PMTM's static deflection displacement.

Kirchhoff's first law of magnetic circuits states that any node in a magnetic circuit has an algebraic sum of zero magnetic flux. Equations (1)~(8) illustrate how the equations were established using the eight nodes in Figure 2.

$$\gamma_6\phi_6 = \phi_7 + \phi_1 \tag{1}$$

$$\phi_1 = \phi_2 + \phi_{10} \tag{2}$$

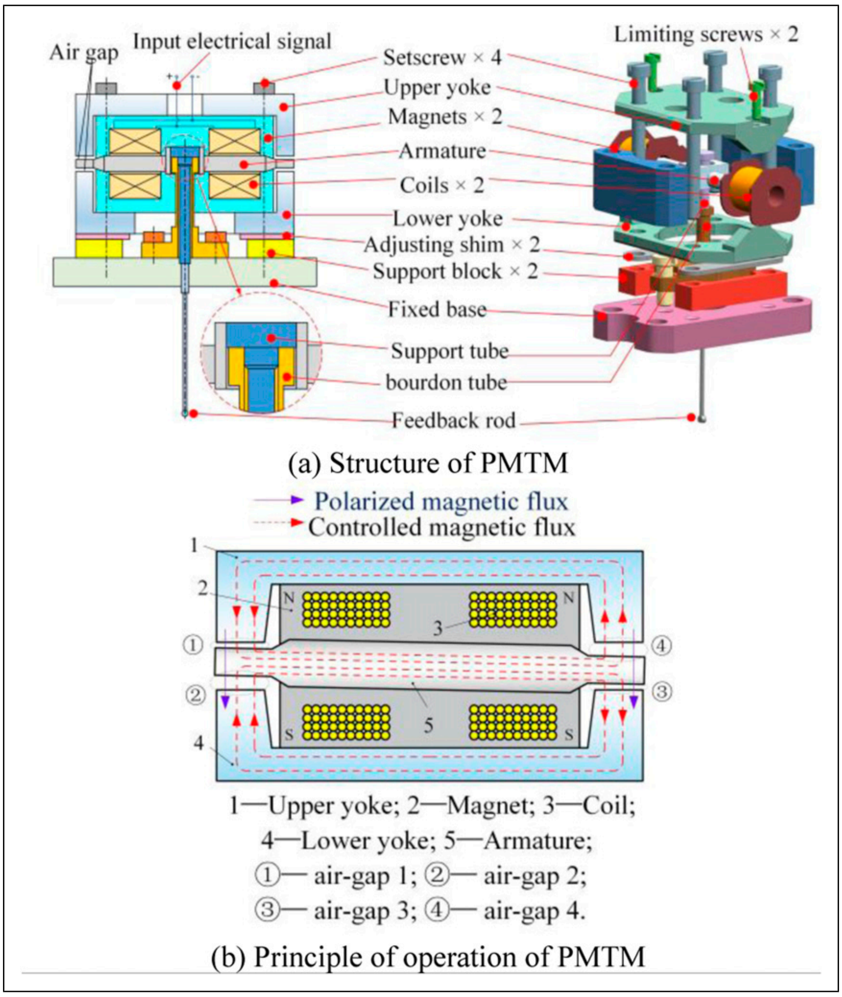

Figure 1. Structure of PMTM and principle of operation.

$$\phi_9 = \phi_7 + \phi_8 \tag{3}$$

$$\phi_{11} + \phi_{12} = \phi_9 + \phi_{10} \tag{4}$$

$$\gamma_5\phi_5 = \phi_8 + \phi_4 \tag{5}$$

$$\phi_3 = \phi_{11} + \phi_4 \tag{6}$$

$$\phi_{12} = \phi_{13} + \phi_{14} \tag{7}$$

$$\gamma_5\phi_5 = \phi_3 + \phi_{14} \tag{8}$$

Kirchhoff's second law of the magnetic circuit states that the algebraic sum of the magnetic potential is equal to the algebraic sum of the magnetic potential drops for any loop in the magnetic circuit. The equations indicated in equations (9)~(14) were established using the six closed loops in Figure 2.

$$M_0 = R_m\phi_6 + \gamma_1 R_{g1}\phi_1 + \gamma_2 R_{g2}\phi_2 \tag{9}$$

$$M_0 = R_m\phi_5 + \gamma_4 R_{g4}\phi_4 + \gamma_3 R_{g3}\phi_3 \tag{10}$$

$$2\gamma_c N_c i = R_{a1}\phi_{10} + R_{a2}\phi_{11} - \gamma_4 R_{g4}\phi_4 + \gamma_1 R_{g1}\phi_1 \tag{11}$$

$$2\gamma_c N_c i = R_{a1}\phi_{10} + R_{a2}\phi_{11} + \gamma_3 R_{g3}\phi_3 - \gamma_2 R_{g2}\phi_2 \tag{12}$$

$$\gamma_c N_c i = R_{a1}\phi_{10} - R_{ng1}\phi_9 + \gamma_1 R_{g1}\phi_1 \tag{13}$$

$$\gamma_c N_c i = R_{a2}\phi_{11} - R_{ng2}\phi_{12} + \gamma_3 R_{g3}\phi_3 \tag{14}$$

Where $\phi_1 \sim \phi_{14}$ are the fluxes through magnetic elements, M_0 is the magnetic potential of the permanent magnet, $M_0 = B_r l_m/\mu_m$, B_r is the remanent magnetism of the permanent magnets, l_m is the effective length of the permanent magnets, μ_m is the magnetic permeability of the permanent magnets, $\mu_m = \mu_0\mu_p$, μ_0 is the air permeability, $\mu_0 = 4\pi\times10^{-7}$ H/m, μ_p is the relative recoil permeability of the

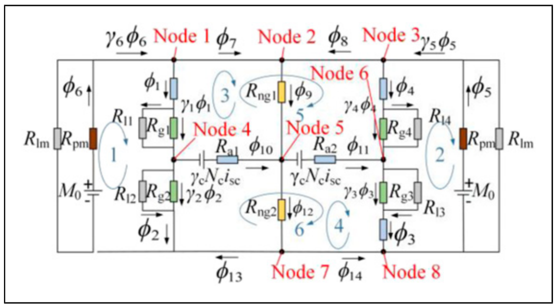

Figure 2. Equivalent magnetic circuit of PMTM.

Table 1. Main parameters of PMTM.

Parameter	Value
Turn of a single coil N_c	950
Remanent magnetism of the permanent magnets B_r (T)	0.58
Relative recoil permeability of permanent magnets μ_p	2
Cross-sectional area of permanent magnets A_m (mm^2)	90.96
Length of the permanent magnets l_m (mm)	10.4
Resistance of non-working air-gap 1 R_{ng1} (H^{-1})	4.0 × 10^7
Resistance of non-working air-gap 2 R_{ng2} (H^{-1})	1.0 × 10^8
Effective area of the armature pole surface A_g (mm^2)	11.1
Rotation radius of the armature r_a (mm)	15
Flux leakage coefficients of the permanent magnets γ_m	0.205
Flux leakage coefficients of the coils γ_c	0.75
Flux leakage coefficients of the air-gaps $\gamma_{i(i=1\sim4)}$	0.855

permanent magnets, N_c is the number of turns per coil, i is the control current in the single coil, R_m is the resistance of the permanent magnets, R_{lm} is the resistance of outside air that is connected to the permanent magnets, R_{a1} and R_{a2} are the resistances of the left and right halves of the armature, respectively, R_{g1}~R_{g4} are the resistances of working air-gaps 1~4, respectively, R_{ng1} and R_{ng2} are the resistances of two non-working air-gaps, and γ_c is the flux leakage coefficient of the control coils. The flux leakage coefficients of the permanent magnets (γ_5 and γ_6) are constants, so $\gamma_5 = \gamma_6 = \gamma_m$ can be set.

The electromagnetic torque T_{tm} of PMTM can be given as

$$T_{tm} = \frac{r_a\left[(\gamma_1\phi_1)^2 - (\gamma_2\phi_2)^2 + (\gamma_3\phi_3)^2 - (\gamma_4\phi_4)^2\right]}{2A_g\mu_0} \quad (15)$$

Where r_a is the rotation radius of the armature, γ_i (i = 1~4) is the flux leakage coefficient of four air gaps, and A_g is the effective area of the pole surfaces of the yoke.

A physical model of the electromagnetic torque of PMTM is established by equations (1)~(15). The exact values of the parameters are listed in Table 1.

Surrogate model of electromagnetic torque

Nevertheless, it is difficult to obtain an explicit equation for the zero-bias of PMTM due to the complex physical model of static electromagnetic torque given by equations (1)~(15), and it is not possible to predict the zero-bias of PMTM. Therefore, in order to establish an explicit zero-bias model for PMTM, a surrogate model of electromagnetic torque must be used. Based on references[10–13], the relationship between electromagnetic torque T_{tm}, armature deflection angle θ_a, and input current i_c may be expressed as follows, assuming that the four initial air gaps of the PMTM are exactly symmetrical and equal to the ideal values.

$$T_{tm} = K_t i_c + K_m\theta_a \quad (16)$$

Where K_t (units: N·m/A) and K_m (units: N·m/rad) are the electromagnetic torque constant and magnetic bourdon stiffness, respectively, and θ_a is the deflection angle.

In actuality, even if both i_c and θ_a are zero, the armature nevertheless experiences electromagnetic torque ($T_{tm}\neq0$) due to the initial asymmetric air gap. Hence, a novel expression of static electromagnetic torque can be presented.

$$T_{tm} = T_{tm0} + K_t i_c + K_m\theta_a \quad (17)$$

We assume that T_{tm0}, K_t, and K_m are functions with the four air gaps X_{gi} (i = 1~4) and remanent magnetism B_r as independent variables, respectively, since the electromagnetic torque model of PMTM is directly related to the four air gaps X_{gi} (i = 1~4) and remanent magnetism B_r.

$$T_{tm0} = T_{tm0}\left(X_{g1}, X_{g2}, X_{g3}, X_{g4}, B_r\right) \quad (18)$$

$$K_t = K_t\left(X_{g1}, X_{g2}, X_{g3}, X_{g4}, B_r\right) \quad (19)$$

$$K_t = K_t\left(X_{g1}, X_{g2}, X_{g3}, X_{g4}, B_r\right) \quad (20)$$

To derive equations (18)~(20), the concept of second-order response surface polynomials is introduced further.

$$Y_\theta(X) = a_0 + \sum_{i=1}^{4} a_i X_i + \sum_{ij(i<j)}^{4} a_{ij} X_i X_j + \sum_{i=1}^{4} a_{ii} X_i^2 \quad (21)$$

Where a_0、a_i、a_{ii}、a_{ij} are the undetermined coefficients of the second-order response surface surrogate model.

To obtain the expressions of T_{tm0}, K_t, and K_m, we first assume that B_r is a fixed value, B_r = 0.58 T, which is obtained by Ref. 17. Next, we suppose that X_{g1}, X_{g2}, X_{g3}, and X_{g4} (units: m) are the input variables X_i (i = 1~4) of equation (21), and the output variables $Y_0(X_i)$ of equation (21) are $T_{tm0}(X_{g1}, X_{g2}, X_{g3}, X_{g4}, B_r)|_{Br=0.58T}$, (units: N·m), $K_t(X_{g1}, X_{g2}, X_{g3}, X_{g4}, B_r)|_{Br=0.58T}$(units: N·m/A), and $K_m(X_{g1}, X_{g2}, X_{g3}, X_{g4}, B_r)|_{Br=0.58T}$(units: N·m/rad), respectively. We set the range of variation of the input variables X_{g1}, X_{g2}, X_{g3}, and X_{g4} to (320~340) μm since the ideal value of the air gap is 330 μm. Four sets of 10,000 air gap samples are extracted within this range. Lastly, the $T_{tm0}(X_{g1}, X_{g2}, X_{g3}, X_{g4}, B_r)|_{Br=0.58T}$, $K_t(X_{g1}, X_{g2}, X_{g3}, X_{g4}, B_r)|_{Br=0.58T}$, and $K_m(X_{g1}, X_{g2}, X_{g3}, X_{g4}, B_r)|_{Br=0.58T}$ can be derived by identifying the electromagnetic torque physical

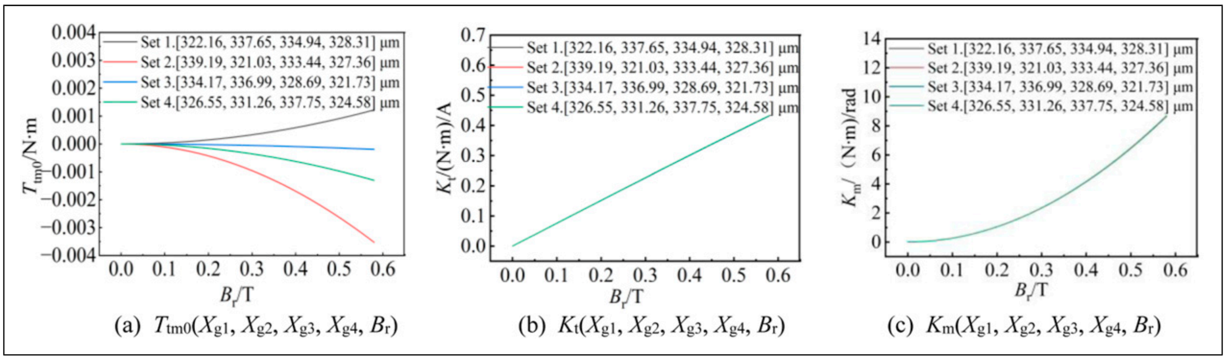

Figure 3. The variation of T_{tm0}, K_t, and K_m with respect to B_r under any four air gaps, respectively.

model built by equations (1)~(15), as shown in Figure A.1 and equations (A.1)~(A.3) of the Appendix.

Similarly, Latin hypercube sampling yields four groups of air gap combinations in (320~340) μm. The results calculated by the physical model of T_{tm0}, K_t, and K_m at various B_r are shown in Figure 3 when we set the variation range of B_r to be (0.01~0.6)T.

Additionally, we nondimensionalize the results of T_{tm0}, K_t, and K_m, which are defined as $T_{tm0}{}^n$, $K_t{}^n$, and $K_m{}^n$, respectively, as shown by equations (22)~(24). The results of $T_{tm0}{}^n$, $K_t{}^n$, and $K_m{}^n$ at varied B_r are compared in Figure 4. $T_{tm0}{}^n$, $K_t{}^n$, and $K_m{}^n$ are found to be only associated with remanent magnetism B_r and independent of the four asymmetric initial air gaps, X_{g1}, X_{g2}, X_{g3}, and X_{g4}. This work shows that the effects of B_r and X_{gi} on $T_{tm0}{}^n$, $K_t{}^n$, and $K_m{}^n$ are independent of each other.

$$T_{tm0}^{n} = \frac{T_{tm0}\left(X_{g1}, X_{g2}, X_{g3}, X_{g4}, B_r\right)}{T_{tm0}\left(X_{g1}, X_{g2}, X_{g3}, X_{g4}, B_r\right)\big|_{B_r=0.58T}} \tag{22}$$

$$K_{t}^{n} = \frac{K_{t}\left(X_{g1}, X_{g2}, X_{g3}, X_{g4}, B_r\right)}{K_{t}\left(X_{g1}, X_{g2}, X_{g3}, X_{g4}, B_r\right)\big|_{B_r=0.58T}} \tag{23}$$

$$K_{m}^{n} = \frac{K_{m}\left(X_{g1}, X_{g2}, X_{g3}, X_{g4}, B_r\right)}{K_{m}\left(X_{g1}, X_{g2}, X_{g3}, X_{g4}, B_r\right)\big|_{B_r=0.58T}} \tag{24}$$

Based on the finding above, the equations (22)~(24) can be further rewritten as

$$T_{tm0}\left(X_{gi}, B_r\right) = T_{tm0}\left(X_{gi}, B_r\right)\big|_{B_r=0.58T} \cdot T_{tm0}^{n} \tag{25}$$

$$K_{t}\left(X_{gi}, B_r\right) = K_{t}\left(X_{gi}, B_r\right)\big|_{B_r=0.58T} \cdot K_{t}^{n} \tag{26}$$

$$K_{m}\left(X_{gi}, B_r\right) = K_{m}\left(X_{gi}, B_r\right)\big|_{B_r=0.58T} \cdot K_{m}^{n} \tag{27}$$

Where the specific expressions of $T_{tm0}{}^n$, $K_t{}^n$, and $K_m{}^n$ can be fitted from Figure 4.

$$T_{tm0}^{n} = T_{tm0}^{n}(B_r) = 1.65 \times e^{-\frac{1}{2}\times\left(\frac{B_r-0.89358}{0.32873}\right)^2} - 0.0529 \tag{28}$$

$$K_{t}^{n} = K_{t}^{n}(B_r) = 1.73 \times B_r + 0.00425 \tag{29}$$

$$K_{m}^{n} = K_{m}^{n}(B_r) = 1.66 \times e^{-\frac{1}{2}\times\left(\frac{B_r-0.89696}{0.32901}\right)^2} - 0.0533 \tag{30}$$

Based on equations (25)~(30), the surrogate model of static electromagnetic torque for a single PMTM can be given as

$$T_{tm} = T_{tm0}\left(X_{gi}, B_r\right) + K_t\left(X_{gi}, B_r\right) \cdot i_c + K_m\left(X_{gi}, B_r\right) \cdot \theta_a \tag{31}$$

Surrogate model of static output displacement

The surrogate model of static deflection displacement of PMTM at room temperature can be given as

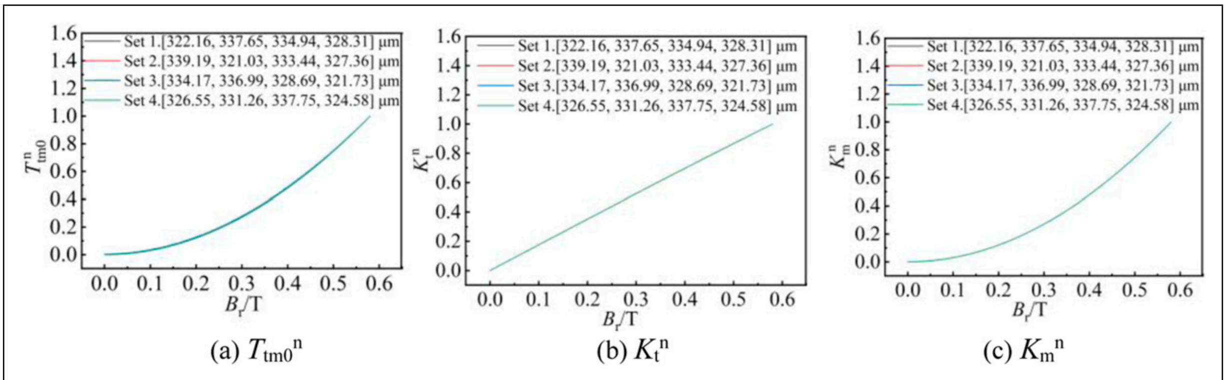

Figure 4. Dimensionless results of $T_{tm0}(X_{g1}, X_{g2}, X_{g3}, X_{g4}, B_r)$, $K_t(X_{g1}, X_{g2}, X_{g3}, X_{g4}, B_r)$ and $K_m(X_{g1}, X_{g2}, X_{g3}, X_{g4}, B_r)$.

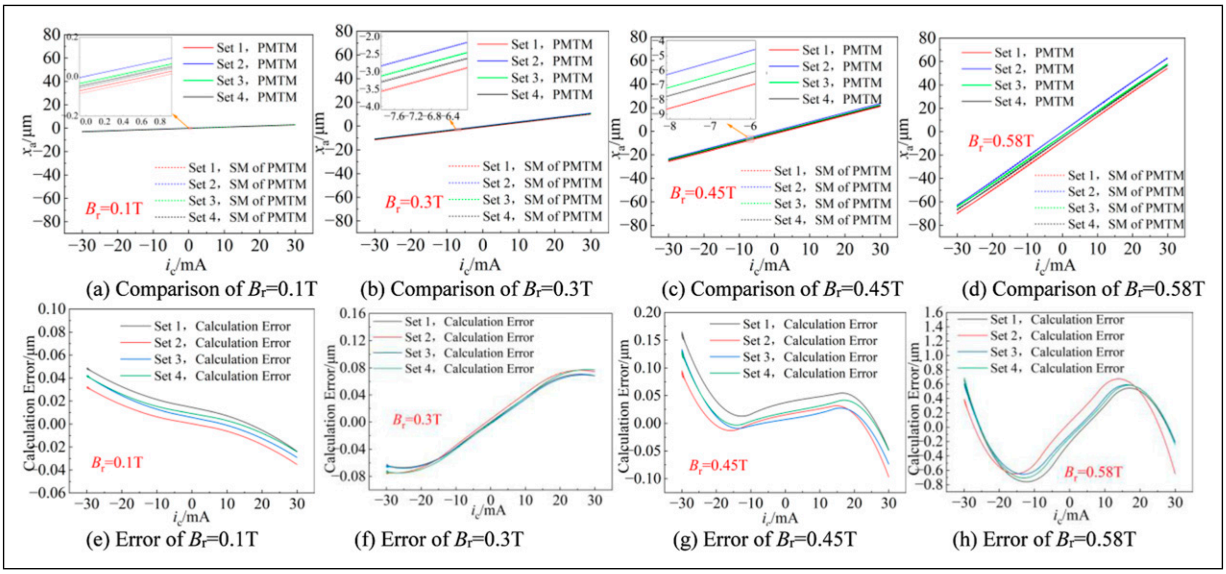

Figure 5. Computational accuracy and error between the surrogate model and physical model of deflection displacement of PMTM.

$$T_{\mathrm{tm}} = T_{\mathrm{tm0}}\left(X_{gi}, B_{\mathrm{r}}\right) + K_{\mathrm{t}}\left(X_{gi}, B_{\mathrm{r}}\right) \cdot i_{\mathrm{c}} + K_{\mathrm{m}}\left(X_{gi}, B_{\mathrm{r}}\right) \cdot \theta_{\mathrm{a}} = K_{\mathrm{tube}}\theta_{\mathrm{a}} \tag{32}$$

Where K_{tube} is the bourdon tube stiffness, θ_{a} is the deflection angle, $\theta_{\mathrm{a}} = x_{\mathrm{a}}/r_{\mathrm{a}}$, and x_{a} is the deflection displacement.

Figure 5 illustrates the computational inaccuracy of the static displacement of PMTM between the surrogate model created by equation (32) and the physical model built by equations (1)–(15). The findings reveal that the relative computational errors of the displacement of PMTM of both models are within 1 μm. This proves that equation (32) can be effectively used as an alternative to the complex physical model to derive subsequent explicit expressions of zero-bias for PMTM.

To further validate the above conclusions, we examine the comparative results and inaccuracy of the physical model and the surrogate model for the PMTM's static deflection displacement at various temperatures. Figure 6 shows that the static deflection displacement curves calculated by the physical model and the surrogate model at different temperatures are essentially the same, with errors within 1.5 μm. This finding also demonstrates that the static surrogate model of PMTM at high temperatures can

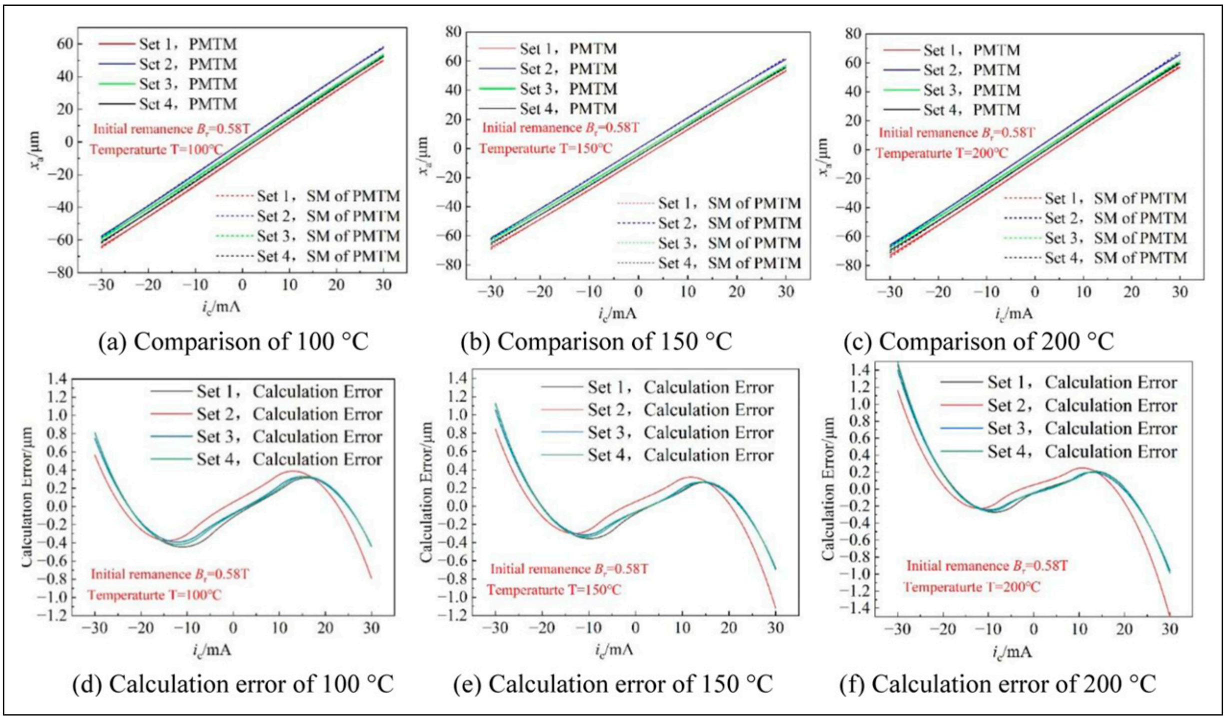

Figure 6. Calculation results and errors of the physical model and the surrogate model under high temperatures.

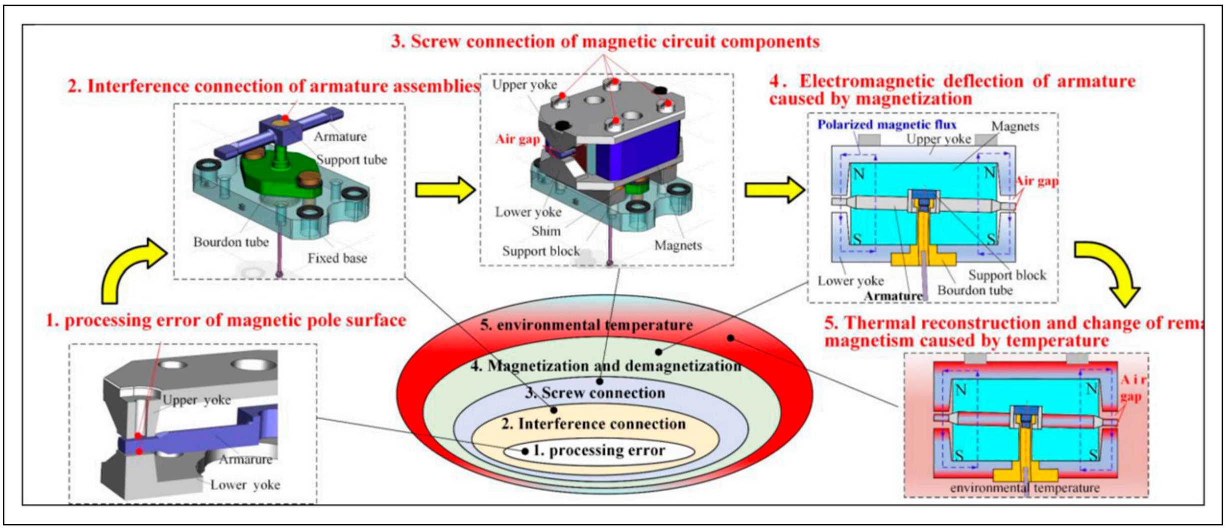

Figure 7. Air gap disturbance factors of PMTM.

accurately replace the static physical model of PMTM at high temperatures.

The Appendix's Figure A.2 and equations (A.4) and (A.6) provide the prediction accuracy of the third-order response surface surrogate model. The results reveal that the prediction accuracy of the second-order response surface for estimating the output displacement of the PMTM is adequate.

Besides, Figure 5 shows that regardless of the air-gap perturbation, the static displacement curve of PMTM remains a straight line at any B_r. Its equation is uniquely given by the zero (i_{tm0}, 0) and slope dx_a/di_c. i_{tm0} denotes the zero-bias current at $x_a = 0$. The slope dx_a/di_c represents the output displacement gain of PMTM. As the temperature rises, the initial four air gaps (X_{g1}, X_{g2}, X_{g3}, and X_{g4}), remanent magnetism B_r, and Bourdon tube stiffness (K_{tube}) change. We define the above variables at T individually as $X_{g1}{}^T$, $X_{g2}{}^T$, $X_{g3}{}^T$, $X_{g4}{}^T$, $B_r{}^T$,[19] and $K_{tube}{}^T$. While $X_{g1}{}^T$, $X_{g2}{}^T$, $X_{g3}{}^T$, and $X_{g4}{}^T$ are PMTM's four air gaps following thermoset coupling expansion, the armature has no electromagnetic deflection. Note that the superscript T of variables is uniformly used to signify the thermal effect, but those without it are all at 20°C.

Referring to equation (32), the surrogate model of static displacement of PMTM at temperature T can be given as

$$\begin{aligned} T_{tm0}^T\left(X_{gi}^T, B_r^T\right) + K_t^T\left(X_{gi}^T, B_r^T\right)\cdot i_c \\ + K_m^T\left(X_{gi}^T, B_r^T\right)\cdot\theta_a = K_{tube}^T\cdot\theta_a \end{aligned} \tag{33}$$

In summary, equations (32) and (33) describe the surrogate models of PMTM static properties at room temperature and high temperature, respectively, and serve as the foundation for the later creation of the zero-bias model of PMTM.

Zero-bias prediction model for PMTM

Connotation of zero bias and air gap disturbance factors

According to the definition of zero-bias of the electro-hydraulic servo valve, the ratio of zero bias current i_{tm0} to the rated current i_{rc} is zero bias.

$$Z_{tm} = \frac{i_{tm0}}{i_{rc}} \times 100\% \tag{34}$$

When the zero-bias current i_{tm0} is input to PMTM, θ_a should be equal to 0. That is, the torque generated by zero-bias current and the T_{tm0} are offset. Based on equations (25) and (26), and substituting the i_{tm0} into equation (32) when θ_a is equal to 0, the zero-bias Z_{tm} at room temperature and the zero-bias $Z_{tm}{}^T$ at temperature T for PMTM can be given as, respectively.

$$\begin{aligned} Z_{tm} &= \frac{i_{tm0}}{i_{rc}}\times 100\% = -\frac{T_{tm0}}{K_t\cdot i_{rc}} \\ &= -\frac{T_{tm0}\left(X_{g1}, X_{g2}, X_{g3}, X_{g4}, B_r\right)}{K_t\left(X_{g1}, X_{g2}, X_{g3}, X_{g4}, B_r\right)\cdot i_{rc}}\times 100\% \end{aligned} \tag{35}$$

$$Z_{tm}^T = -\frac{T_{tm0}^T}{K_t^T\cdot i_{rc}} = -\frac{T_{tm0}^T\left(X_{g1}^T, X_{g2}^T, X_{g3}^T, X_{g4}^T, B_r^T\right)}{K_t^T\left(X_{g1}^T, X_{g2}^T, X_{g3}^T, X_{g4}^T, B_r^T\right)\cdot i_{rc}}\times 100\% \tag{36}$$

According to servo valve performance indicators, the zero-bias should not exceed 3%, which is strongly tied to fluctuations in the initial four air gaps (X_{g1}, X_{g2}, X_{g3}, and X_{g4}). Figure 7 depicts the elements that influence the four air gaps of PMTM. These factors include processing errors on the yoke and armature's magnetic pole surfaces, interference fits between the

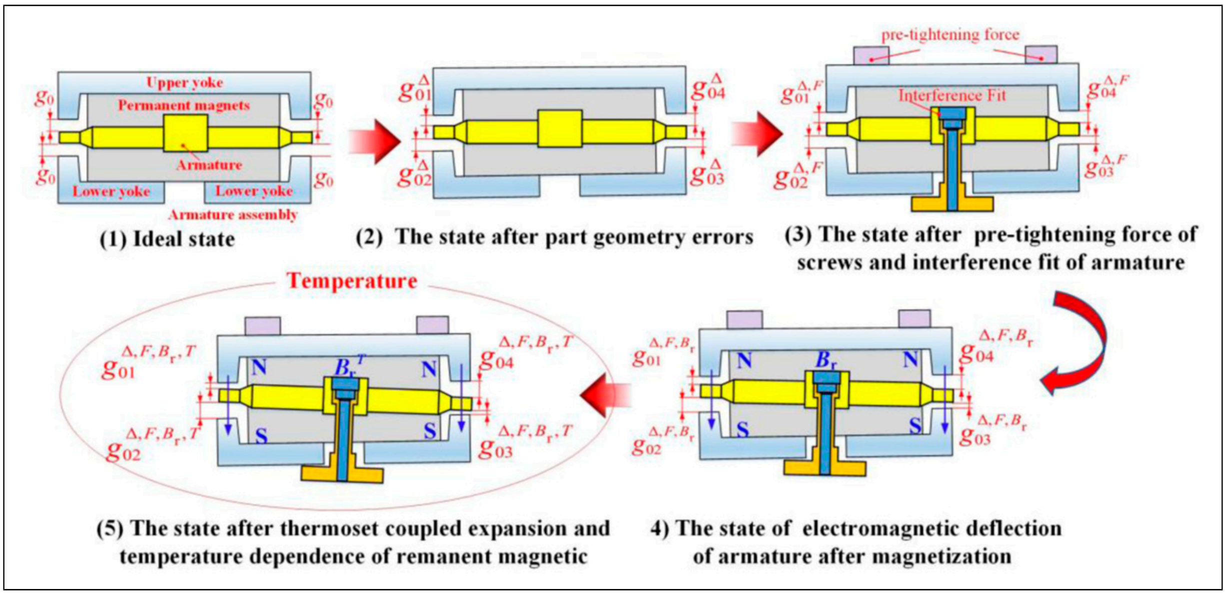

Figure 8. The perturbation form of air-gap length.

armature and support tube, screw connections of magnetic circuit components, electromagnetic deflection of the armature caused by magnetization, thermal reconstruction, and temperature-induced magnetism changes. In conclusion, these factors considerably break the symmetry of the four air gaps, causing the zero-bias of PMTM or servo valves to exceed the required limitations.

Figure 8 illustrates the generation mechanism of the effect of the above factors from Figure 7 on air gap disturbance: As shown in Figure 8(1), the initial air gap in this state exhibits perfect symmetry, with the design value g_0. As shown in Figure 8(2), the effect of the processing error of the magnet pole face on the air gap was further considered in this state, denoted by $g_{01}{}^{\Delta} \sim g_{04}{}^{\Delta}$. The superscript Δ denotes taking the magnetic pole

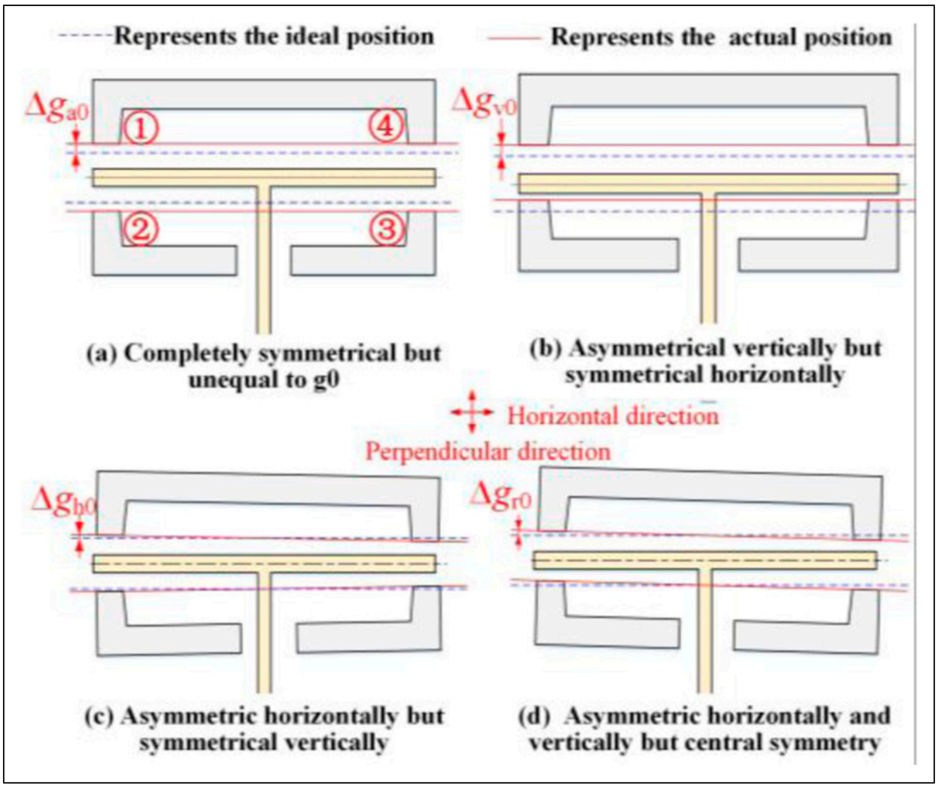

Figure 9. The perturbation form of air-gap length.

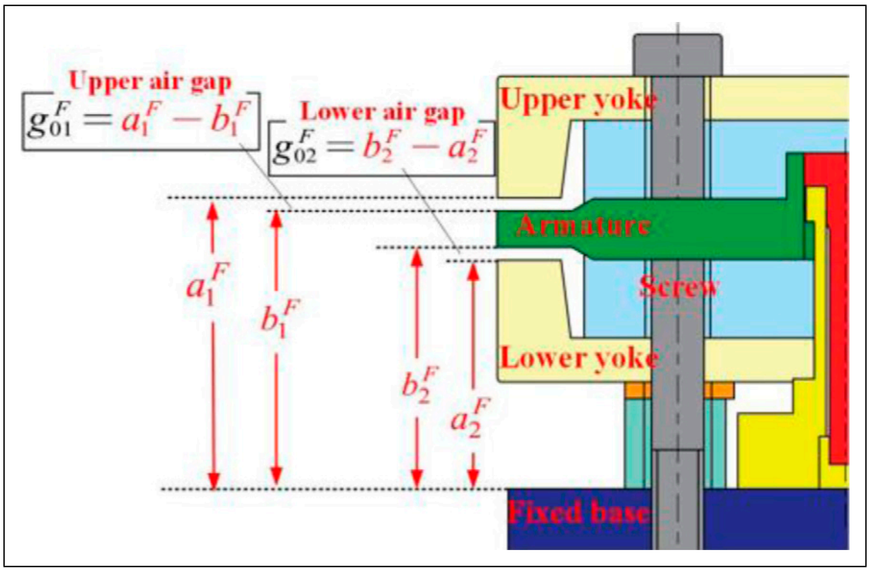

Figure 10. The upper and lower air gap model caused by the connection of interference and screws at 20°C.

surface's machining imperfection into account. As shown in Figure 8(3), the connection force of pre-tightening and interference is further considered in this state, denoted by $g_{01}^{\Delta, F} \sim g_{04}^{\Delta, F, Br}$. The superscript F denotes taking the connection force. As shown in Figure 8(4), the electromagnetic deflection of the armature is further considered in this state, denoted by $g_{01}^{\Delta, F, Br} \sim g_{04}^{\Delta, F, Br}$. The superscript B_r denotes taking into account the armature's electromagnetic deflection brought on by magnetization. As shown in Figure 8(5), the effect of temperature on thermal deformation and magnetism is further considered, denoted by $g_{01}^{\Delta, F, Br, T} \sim g_{04}^{\Delta, F, Br, T}$. The superscript T denotes taking into account how temperature affects magnetic temperature change and thermo-solid coupling.

To summarize, in order to achieve the precise expression of the zero-bias model of PMTM, the air gap disturbance model must be established first. As a result, Sections 3.2 and 3.3 provide explicit expressions for the air gap disturbance model of the proposed disturbance factors.

Air gap disturbance model at room temperature

As shown in Figure 8(2), the air gap disturbance model $g_{0i}^{\Delta}(g_{0i}^{\Delta} = g_{0i} + \Delta g_{0i}^{\Delta}$, $i = 1 \sim 4)$ caused by processing errors of the magnet pole face can be regarded as four forms in Figure 9. The g_{0i} is the ideal value g_0. It is assumed that the perturbation causing an increase in the length of the air gap is positive. For the four forms in Figure 9, we can get four models.

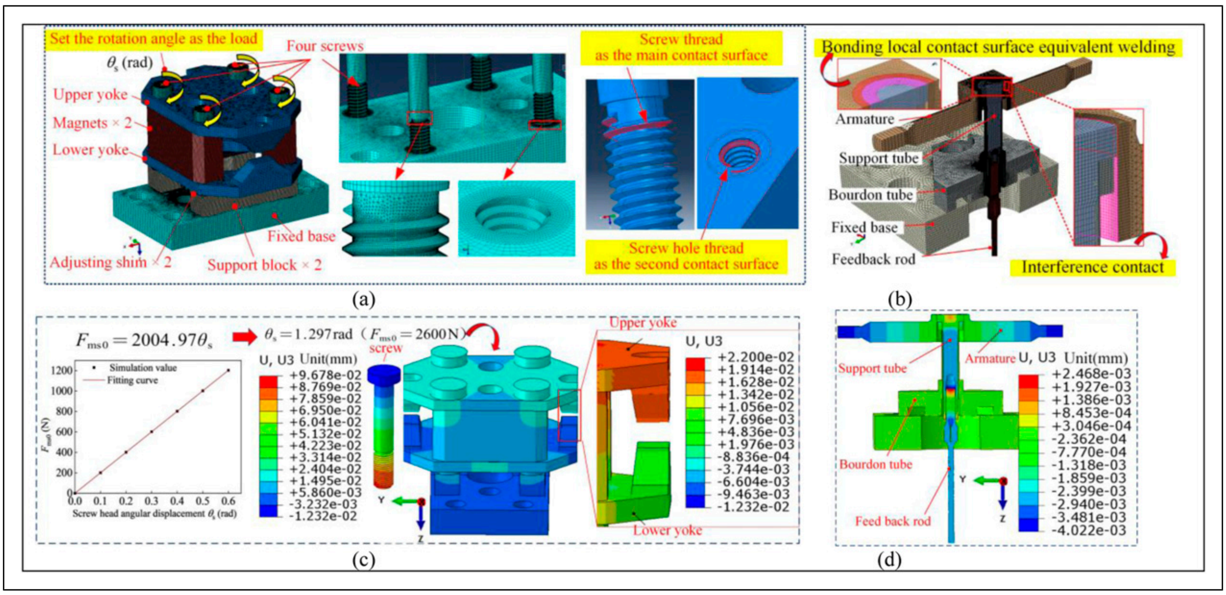

Figure 11. FEA mesh model of PMTM in ABAQUS and simulation results at 20°C.

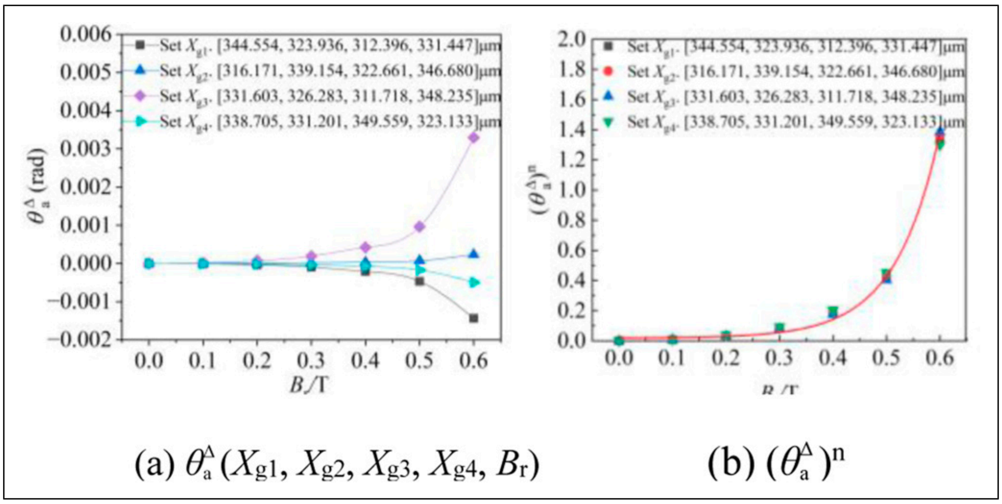

Figure 12. The variation of θ_a^Δ and normalized results.

$$\begin{bmatrix} g_{01}^\Delta \\ g_{02}^\Delta \\ g_{03}^\Delta \\ g_{04}^\Delta \end{bmatrix} = \begin{bmatrix} g_{01} + \Delta g_{a0} \\ g_{02} + \Delta g_{a0} \\ g_{03} + \Delta g_{a0} \\ g_{04} + \Delta g_{a0} \end{bmatrix} = \begin{bmatrix} g_{01} + \Delta g_{v0} \\ g_{02} - \Delta g_{v0} \\ g_{03} - \Delta g_{v0} \\ g_{04} + \Delta g_{v0} \end{bmatrix} = \begin{bmatrix} g_{01} + \Delta g_{h0} \\ g_{02} + \Delta g_{h0} \\ g_{03} - \Delta g_{h0} \\ g_{04} - \Delta g_{h0} \end{bmatrix} = \begin{bmatrix} g_{01} + \Delta g_{r0} \\ g_{02} - \Delta g_{r0} \\ g_{03} + \Delta g_{r0} \\ g_{04} - \Delta g_{r0} \end{bmatrix} \tag{37}$$

where Δg_{a0}, Δg_{v0}, Δg_{h0}, and Δg_{r0} represent the average perturbation, the vertical perturbation, the horizontal perturbation, and the rotation direction perturbation, respectively, of the air-gap lengths. According to equation (37), the change in air gap compared to the ideal value induced by processing errors on the magnet pole face is

$$\begin{bmatrix} \Delta g_{01}^\Delta \\ \Delta g_{02}^\Delta \\ \Delta g_{03}^\Delta \\ \Delta g_{04}^\Delta \end{bmatrix} = \begin{bmatrix} g_{01}^\Delta - g_{01} \\ g_{02}^\Delta - g_{02} \\ g_{03}^\Delta - g_{03} \\ g_{04}^\Delta - g_{04} \end{bmatrix} = \begin{bmatrix} 1 & 1 & 1 & 1 \\ 1 & -1 & 1 & -1 \\ 1 & -1 & -1 & 1 \\ 1 & 1 & -1 & -1 \end{bmatrix} \begin{bmatrix} \Delta g_{a0} \\ \Delta g_{v0} \\ \Delta g_{h0} \\ \Delta g_{r0} \end{bmatrix} \tag{38}$$

Under the actual processing conditions of PMTM, we typically limit the processing errors of the magnet pole face on the air gap, i.e., $\Delta g_{0i}^\Delta \leq Err\_\Delta g_{0i}^\Delta (i = 1 \sim 4)$.

As seen in Figure 10, the subtraction of a_1^F and a_2^F, b_1^F and b_2^F, yields the upper and lower air gap perturbation models g_{01}^F and g_{02}^F of PMTM induced by the connection of interference and screws at 20°C.

Pre-tightening force and armature interference, denoted a_1^F and a_2^F, and b_1^F and b_2^F, are taken into consideration while modeling the positions of the yoke's magnetic pole surface and the armature in relation to the top surface of the fixed base. Figure 11(a) and (b) displays the FEA mesh models of armature assemblies and magnetic circuit assemblies using the ABAQUS platform. The predicted cloud diagram for vertical displacement at 20°C is shown in Figure 11(c) and (d).

The a_1^F and a_2^F, b_1^F and b_2^F, can be obtained as follows by fitting the simulation results of Figure 11(c) and (d):

$$\begin{cases} a_1^F = a_1 - \Delta a_1^F = a_1 - 4F_{ms0}/k_{mf1} \\ a_2^F = a_2 - \Delta a_2^F = a_1 - 4F_{ms0}/k_{mf2} \\ b_1^F = 0.0132699 - 0.82\delta_{int} = b_1 - \Delta b_1^F \\ b_2^F = 0.0115298 - 0.74\delta_{int} = b_2 - \Delta b_2^F \\ g_{01}^F = a_1^F - b_1^F = g_0 - \Delta a_1^F + \Delta b_1^F \\ g_{02}^F = b_2^F - a_2^F = g_0 + \Delta a_2^F - \Delta b_2^F \end{cases} \tag{39}$$

where a_1 and a_2 are the ideal sizes of the magnet pole surfaces of the upper and lower yoke in relation to the top surface of the fixed base, respectively; k_{mf1} and k_{mf2} are the equivalent stiffnesses affecting Δa_1^F and Δa_2^F; δ_{int} is the interference fit value of the armature, which affects the Δb_1^F and Δb_2^F, respectively; and b_1 and b_2 are the ideal sizes of the upper and lower magnet pole faces of the armature in relation to the top surface of the fixed base, respectively. We can calculate the $k_{mf1} = 6.05 \times 10^8$ N/m and the $k_{mf2} = 3.03 \times 10^9$ N/m based on the simulation results of Figure 11 on ABAQUS.

Referring to equation (38), the change of air gap relative to the ideal position at 20°C caused by the connection of the interference and screws is

$$\begin{bmatrix} \Delta g_{01}^F \\ \Delta g_{02}^F \\ \Delta g_{03}^F \\ \Delta g_{04}^F \end{bmatrix} = \begin{bmatrix} g_{01}^F - g_{01} \\ g_{02}^F - g_{02} \\ g_{03}^F - g_{03} \\ g_{04}^F - g_{04} \end{bmatrix} = \begin{bmatrix} 1 & 1 & 1 & 1 \\ 1 & -1 & 1 & -1 \\ 1 & -1 & -1 & 1 \\ 1 & 1 & -1 & -1 \end{bmatrix} \begin{bmatrix} \Delta g_a^F \\ \Delta g_v^F \\ \Delta g_h^F \\ \Delta g_r^F \end{bmatrix} \tag{40}$$

Where Δg_a^F, Δg_v^F, Δg_h^F, and Δg_r^F represent the average perturbation, the vertical perturbation, the horizontal

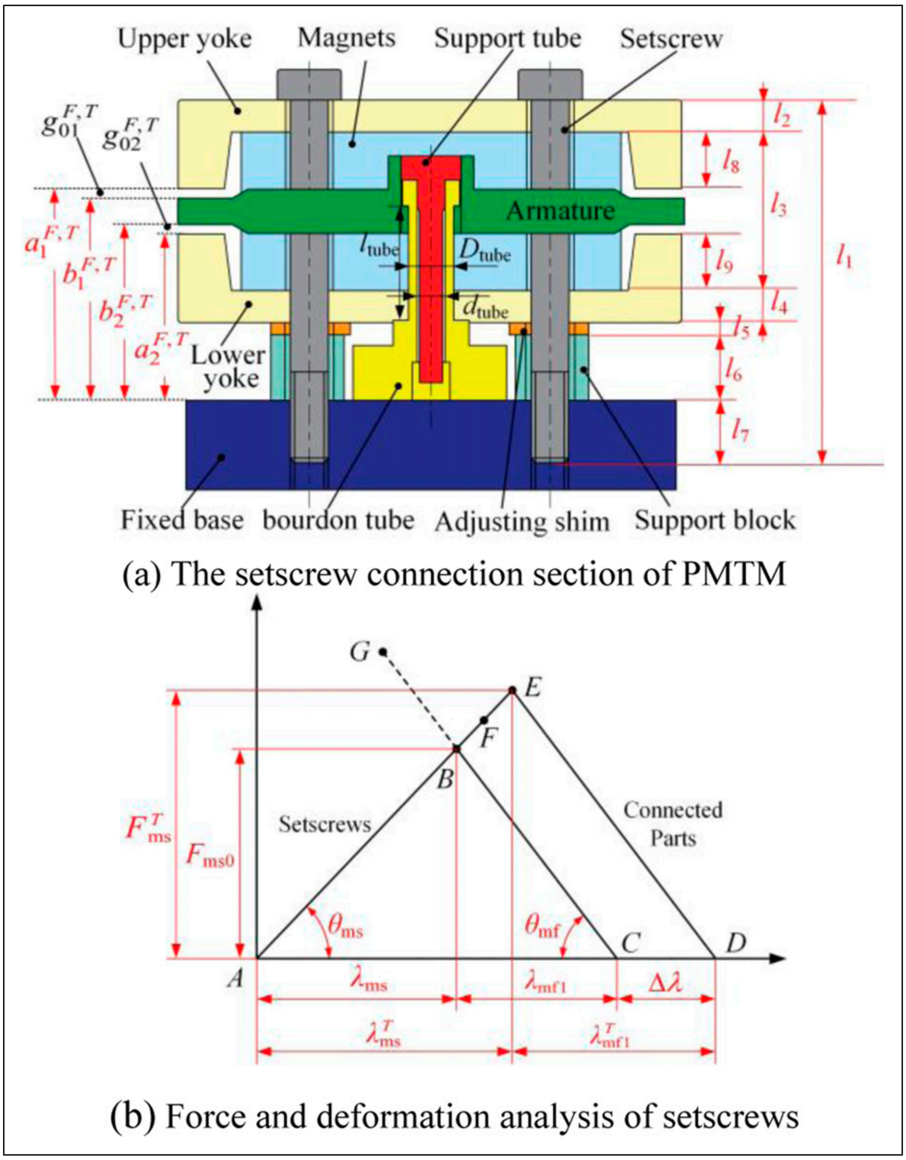

Figure 13. Equivalent stiffness affecting $\Delta a_1{}^F$ and $\Delta a_2{}^F$.

perturbation, and the rotation direction perturbation, respectively, of the air-gap lengths caused by F_{ms0} and δ_{int}.

Considering the symmetry of the structure and pre-tightening force, there are $\Delta g_{01}{}^F = \Delta g_{04}{}^F$ and $\Delta g_{02}{}^F = \Delta g_{03}{}^F$. Adding equations (38) and (40), the air gap disturbance models $g_{01}{}^{\Delta,F} \sim g_{04}{}^{\Delta,F}$ caused by the connection of interference and screw in Figure 8(3) can be given as

$$\begin{bmatrix} g_{01}^{\Delta,F} \\ g_{02}^{\Delta,F} \\ g_{03}^{\Delta,F} \\ g_{04}^{\Delta,F} \end{bmatrix} = \begin{bmatrix} g_{01} \\ g_{02} \\ g_{03} \\ g_{04} \end{bmatrix} + \begin{bmatrix} 1 & 1 & 1 & 1 \\ 1 & -1 & 1 & -1 \\ 1 & -1 & -1 & 1 \\ 1 & 1 & -1 & -1 \end{bmatrix} \cdot \begin{bmatrix} \Delta g_{\mathrm{a0}} + \Delta g_{\mathrm{a}}^F \\ \Delta g_{\mathrm{v0}} + \Delta g_{\mathrm{v}}^F \\ \Delta g_{\mathrm{h0}} + 0 \\ \Delta g_{\mathrm{r0}} + 0 \end{bmatrix} \tag{41}$$

Where $[g_{01}{}^{\Delta,F}, g_{02}{}^{\Delta,F}, g_{03}{}^{\Delta,F}, g_{04}{}^{\Delta,F}]^{\mathrm{T}}$ is the air gap model when PMTM completes the connection of interference and screws, but the permanent magnets are not magnetized.

Following the permanent magnet's magnetization, the armature assemblies deflect at a specific angle in response to the electromagnetic force, which further modifies the PMTM's four air gaps. Consequently, the deflection angle $\theta_{\mathrm{a}}{}^{\Delta}$ of armature assemblies must be determined.

We can suppose that $\theta_{\mathrm{a}}{}^{\Delta}$ functions with four air gaps, X_{g1}, X_{g2}, X_{g3}, and X_{g4}, and B_{r}, by referring to equations (25)~(27).

$$\theta_{\mathrm{a}}^{\Delta} = \theta_{\mathrm{a}}^{\Delta}(X_{\mathrm{g1}}, X_{\mathrm{g2}}, X_{\mathrm{g3}}, X_{\mathrm{g4}}, B_{\mathrm{r}}) \tag{42}$$

Referring to the equations (22)~(24), using second-order response surface polynomials, Figure 12(a) shows the variations of deflection angle of armature assemblies $\theta_{\mathrm{a}}{}^{\Delta}$ with B_{r} under any four combinations of air gaps. Then, we nondimensionalize the calculation results of $\theta_{\mathrm{a}}{}^{\Delta}$.

$$(\theta_{\mathrm{a}}^{\Delta})^{\mathrm{n}} = \frac{\theta_{\mathrm{a}}^{\Delta}(X_{\mathrm{g1}}, X_{\mathrm{g2}}, X_{\mathrm{g3}}, X_{\mathrm{g4}}, B_{\mathrm{r}})}{\theta_{\mathrm{a}}^{\Delta}(X_{\mathrm{g1}}, X_{\mathrm{g2}}, X_{\mathrm{g3}}, X_{\mathrm{g4}}, B_{\mathrm{r}})\big|_{B_{\mathrm{r}}=0.58\mathrm{T}}} \tag{43}$$

Where $(\theta_{\mathrm{a}}{}^{\Delta})^{\mathrm{n}}$ is the dimensionless expression of $\theta_{\mathrm{a}}{}^{\Delta}$.

The dimensionless results of θ_a^{Δ} at any B_r are contrasted to the results at B_r = 0.58 T in Figure 12(b). Similar to the data examined in Figure 4, we can still observe that $(\theta_a^{\Delta})^n$ is simply related to B_r and independent of X_{g1}, X_{g2}, X_{g3}, and X_{g4}. As a result, we can further rewrite equation (43).

$$\theta_a^{\Delta}(X_{gi}, B_r) = (\theta_a^{\Delta})^n \cdot \theta_a^{\Delta}(X_{gi}, B_r)\big|_{B_r=0.58T} = 0.01899 + 0.00194e^{\frac{B_r-0.05402}{0.08331}} \cdot \theta_a^{\Delta}(X_{gi}, B_r)\big|_{B_r=0.58T} \tag{44}$$

The data in Figure 12(b) can be used to fit $(\theta_a^{\Delta})^n$. The appendix contains the result for $\theta_a^{\Delta}(X_{gi}, B_r)|_{Br=0.58T}$(rad).

Substituting $X_{gi} = [\, g_{01}^{\Delta,F}, g_{02}^{\Delta,F}, g_{03}^{\Delta,F}, g_{04}^{\Delta,F}]^T$ of equation (41) into equation (44), we can have

$$\theta_a^{\Delta} = 0.01899 + 0.00194e^{\frac{B_r-0.05402}{0.08331}} \cdot \left\{ \begin{bmatrix} -189.479 + 3.148\times 10^6(\Delta g_{a0} + \Delta g_a^F) \\ -266891.781(\Delta g_{v0} + \Delta g_v^F) \end{bmatrix} \Delta g_{r0} + \begin{bmatrix} 27.703 - 432506.139(\Delta g_{a0} + \Delta g_a^F) \\ +814545.502(\Delta g_{v0} + \Delta g_v^F) \end{bmatrix} \Delta g_{h0} \right\} \tag{45}$$

Figure 9(d) illustrates that the armature's deflection angle θ_a^{Δ} only causes disturbance along the axis. As shown in Figure 8(4), the air-gap model $g_{01}^{\Delta,F,Br} \sim g_{04}^{\Delta,F,Br}$ is induced by electromagnetic deflection of the armature.

$$\begin{bmatrix} g_{01}^{\Delta,F,B_r} \\ g_{02}^{\Delta,F,B_r} \\ g_{03}^{\Delta,F,B_r} \\ g_{04}^{\Delta,F,B_r} \end{bmatrix} = \begin{bmatrix} g_{01} \\ g_{02} \\ g_{03} \\ g_{04} \end{bmatrix} + \begin{bmatrix} 1 & 1 & 1 & 1 \\ 1 & -1 & 1 & -1 \\ 1 & -1 & -1 & 1 \\ 1 & 1 & -1 & -1 \end{bmatrix} \cdot \begin{bmatrix} \Delta g_{a0} + \Delta g_a^F \\ \Delta g_{v0} + \Delta g_v^F \\ \Delta g_{h0} + 0 \\ \Delta g_{r0} - r_a\theta_a^{\Delta} \end{bmatrix} \tag{46}$$

In actuality, an error range is generally specified for air-gap length, $g_{0i}^{\Delta,F,Br}$, after magnetization.

$$\begin{cases} |g_{01}^{\Delta,F,B_r} - g_{02}^{\Delta,F,B_r}| \leqslant Err\_g_v \\ |g_{03}^{\Delta,F,B_r} - g_{04}^{\Delta,F,B_r}| \leqslant Err\_g_v \\ |g_{01}^{\Delta,F,B_r} - g_{04}^{\Delta,F,B_r}| \leqslant Err\_g_h \\ |g_{02}^{\Delta,F,B_r} - g_{03}^{\Delta,F,B_r}| \leqslant Err\_g_h \end{cases} \tag{47}$$

Where Err_g_v and Err_g_h are the error ranges for controlling the initial air-gap length perturbations in the vertical and horizontal directions, respectively.

Air gap disturbance model at high temperature

As illustrated in Figure 13(a), the upper and lower air gap models $g_{01}^{F,T}$ and $g_{02}^{F,T}$ induced by temperature can be further produced by subtracting the thermal displacement model between magnetic circuit components and armature assemblies (i.e., $g_{01}^{F,T} = a_1^{F,T} - b_1^{F,T}$, $g_{02}^{F,T} = b_2^{F,T} - a_2^{F,T}$). The Appendix's Tables A.1 and A.2 contains a list of the physical-mechanical parameters used in PMTM.

The screw of magnetic circuit components elongates by $\Delta\lambda$ in relation to the fasteners being fastened when the temperature varies by ΔT. The dimensions (i = 1~9) of each component at temperature T can be computed using the free thermal expansion as

$$\begin{cases} l_i^T = l_i + \Delta l_i^T = l_i(1+\alpha_i\Delta T) \\ \Delta\lambda = [\alpha_1 l_1 - (\alpha_2 l_2 + \alpha_3 l_3 + \alpha_4 l_4 + \alpha_5 l_5 + \alpha_6 l_6 + \alpha_7 l_7)]\Delta T \end{cases} \tag{48}$$

Where Δl_i^T is the thermal expansion of the part, $\Delta T = T - T_0 (T_0 = 20°C)$, and α_i is the coefficient of the connected parts of PMTM in Figure 13(a), respectively.

As seen in Figure 13(b), we assume that the screw's deformation at temperature T is λ_{ms}^T and the overall deformation of the fastened parts is λ_{mf1}^T. Hooke's theorem states that since the total pre-tightening force is $4F_{ms0}$, we have

$$\Delta\lambda = \lambda_{ms}^T - \lambda_{ms} + \lambda_{mf1}^T - \lambda_{mf1} = \frac{F_{ms}^T - F_{ms0}}{k_{ms}^T} + \frac{4(F_{ms}^T - F_{ms0})}{k_{mf1}^T} F_{ms}^T = F_{ms0} + \frac{k_{ms}^T k_{mf1}^T}{5(k_{ms}^T + k_{mf1}^T)}\Delta\lambda \tag{49}$$

Where k_{ms}^T and k_{mf1}^T are the equivalent stiffness of a screw and connected parts, respectively, at the temperature T.

It is worth noting that in the preceding derivation procedure, the setscrews and related parts are assumed to be under unidirectional tensile or compressive stress. However, it should be noted that both screws and linked parts undergo diverse stress states. To adjust the thermal displacement of the upper and lower yoke pole surfaces, a correction coefficient (ξ_1 and ξ_2) related to F_{ms0} is required.

$$\begin{cases} \Delta a_1^T = l_3^T + l_4^T + l_5^T + l_6^T - l_8^T - a_1 \\ \Delta a_2^T = l_4^T + l_5^T + l_6^T + l_9^T - a_2 \\ a_1^T = a_1 + \xi_1 \Delta a_1^T \\ a_2^T = a_2 + \xi_2 \Delta a_2^T \end{cases} \tag{50}$$

Then, referring to equation (39), the $a_1^{F,T}$, and $a_2^{F,T}$ in Figure 13(a) can be given as

$$\begin{cases} a_1^{F,T} = a_1^T - 4F_{ms}^T / k_{mf1}^T = a_1 + \Delta T\xi_1\left(\sum_{i=3}^{6}\alpha_i l_i - \alpha_8 l_8\right) - \frac{4F_{ms}^T}{k_{mf1}^T} \\ a_2^{F,T} = a_2^T - 4F_{ms}^T / k_{mf2}^T = a_2 + \Delta T\xi_2\left(\sum_{i=4}^{6}\alpha_i l_i + \alpha_9 l_9\right) - \frac{4F_{ms}^T}{k_{mf2}^T} \end{cases} \tag{51}$$

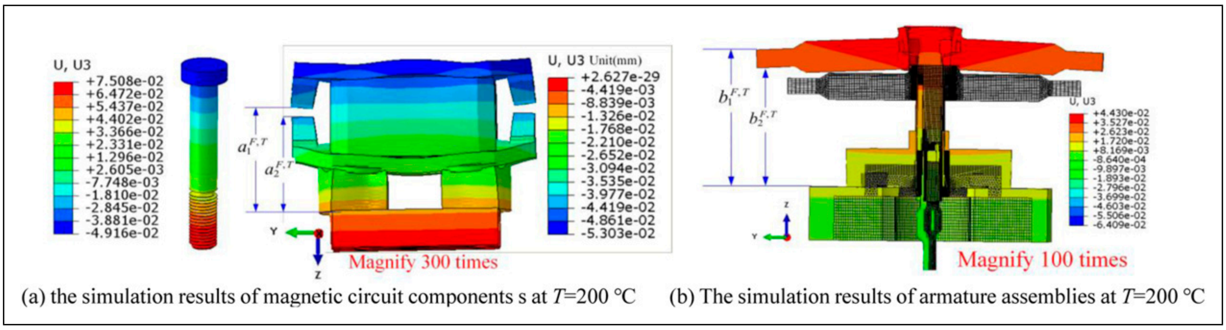

Figure 14. The Cloud image of thermal displacement of PMTM at T = 200°C.

Where $k_{mf2}{}^{T}$ is the equivalent stiffness of the fastened parts.

Each connected part's temperature coefficient of Young's modulus is assumed to be equal to streamline the computation. The $k_{mf1}{}^{T}$ and $k_{mf2}{}^{T}$ can be expressed as

$$\begin{cases} k_{mf1}^{T} = (1+\eta\Delta T)k_{mf1} \\ k_{mf2}^{T} = (1+\eta\Delta T)k_{mf2} \end{cases} \tag{52}$$

Similarly, the thermal displacement of armature assemblies $b_1{}^{F,\,T}$ and $b_2{}^{F,\,T}$ in Figure 13(a) can be given as

$$\begin{cases} b_1^{F,T} = b_1 + \Delta b_1^{F,T} \\ b_2^{F,T} = b_2 + \Delta b_2^{F,T} \end{cases} \tag{53}$$

The temperature displacement simulation results of armature assemblies and magnetic circuit components utilizing the ABAQUS platform are shown in Figure 14. The simulation results obtain the $\xi_1 = 1.23 + 1.81 \times 10^{-5}F_{ms0}$ and $\xi_2 = 1.13 + 1.5 \times 10^{-5}F_{ms0}$. The theoretical and FEA findings of $a_1{}^{F,\,T}$, and $a_2{}^{F,\,T}$, respectively, are shown in Figure 15(a)~(d). The theoretical calculation errors of $a_1{}^{F,\,T}$, and $a_2{}^{F,\,T}$, are both within 2.0 μm between 20°C and 200°C. The FEA findings of the $b_1{}^{F,\,T}$, and $b_2{}^{F,\,T}$, are shown in Figure 15(e) and (f), respectively. The link between $b_1{}^{F,\,T}$, and $b_2{}^{F,\,T}$ at T = 200°C and δ_{int} is yielded by fitting the data, respectively.

$$\begin{cases} b_1^{F,T}|_{T=200^\circ C} = 0.01329665 - 2.01\delta_{int} \\ b_2^{F,T}|_{T=200^\circ C} = 0.01155365 - 2.01\delta_{int} \end{cases} \tag{54}$$

According to Figure 13(a), we can have

$$\begin{cases} g_{01}^{F,T} = a_1^{F,T} - b_1^{F,T} = \\ g_0 + 180 \times \xi_1 \left(\sum_{i=3}^{6} \alpha_i l_i - \alpha_8 l_8 \right) - \dfrac{4F_{ms}^{T}}{k_{mf1}^{T}} - \Delta b_1^{F,T} \\ g_{02}^{F,T} = b_2^{F,T} - a_2^{F,T} = \\ g_0 + \Delta b_2^{F,T} - 180 \times \xi_2 \left(\sum_{i=4}^{6} \alpha_i l_i + \alpha_9 l_9 \right) + \dfrac{4F_{ms}^{T}}{k_{mf2}^{T}} \end{cases} \tag{55}$$

Referring to equation (40), the thermally induced variation in four air gaps with respect to the values at 20°C can be stated as follows:

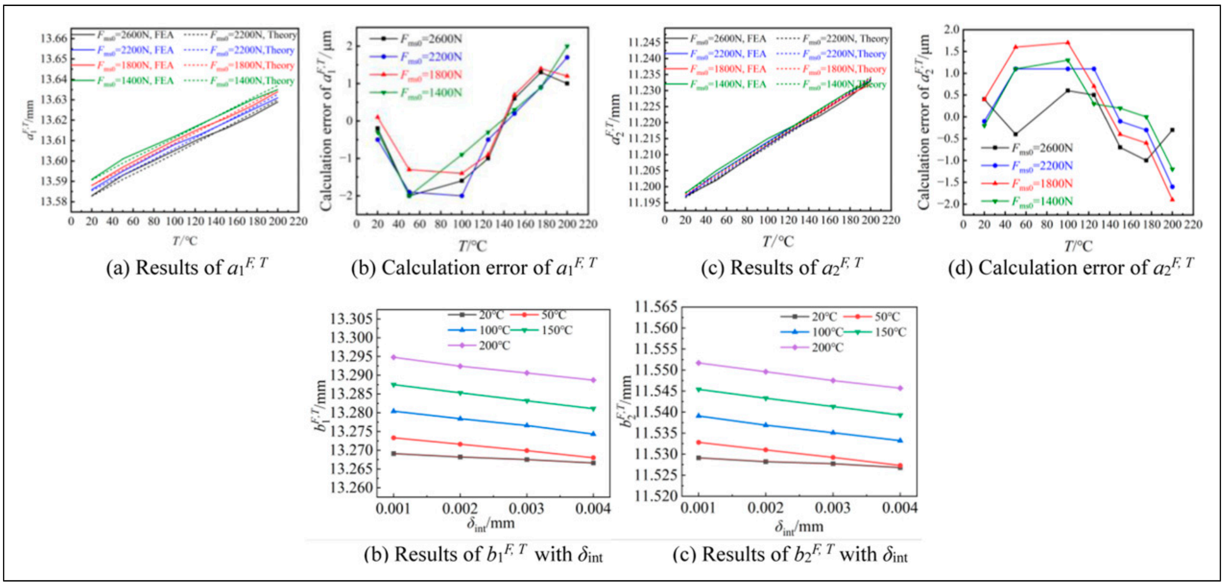

Figure 15. The simulation results of the position of the magnetic pole surface under high temperature.

$$\begin{bmatrix}\Delta g_{01}^{F,T}\\ \Delta g_{02}^{F,T}\\ \Delta g_{03}^{F,T}\\ \Delta g_{04}^{F,T}\end{bmatrix}=\begin{bmatrix}g_{01}^{F,T}-g_{01}^{F}\\ g_{02}^{F,T}-g_{02}^{F}\\ g_{03}^{F,T}-g_{03}^{F}\\ g_{04}^{F,T}-g_{04}^{F}\end{bmatrix}=\begin{bmatrix}1&1&1&1\\1&-1&1&-1\\1&-1&-1&1\\1&1&-1&-1\end{bmatrix}\begin{bmatrix}\Delta g_{a}^{F,T}\\ \Delta g_{v}^{F,T}\\ \Delta g_{h}^{F,T}\\ \Delta g_{r}^{F,T}\end{bmatrix} \tag{56}$$

Where $g_{01}{}^{F}$ and $g_{02}{}^{F}$ come from equation (39).

Then, substituting the $\Delta g_a{}^{F,\ T}$, $\Delta g_v{}^{F,\ T}$, $\Delta g_h{}^{F,\ T}$, and $\Delta g_r{}^{F,\ T}$ into equation (41), we can have

$$\begin{bmatrix}g_{01}^{\Delta,F,T}\\ g_{02}^{\Delta,F,T}\\ g_{03}^{\Delta,F,T}\\ g_{04}^{\Delta,F,T}\end{bmatrix}=\begin{bmatrix}g_0\\g_0\\g_0\\g_0\end{bmatrix}+\begin{bmatrix}1&1&1&1\\1&-1&1&-1\\1&-1&-1&1\\1&1&-1&-1\end{bmatrix}\cdot\begin{bmatrix}\Delta g_{a0}+\Delta g_a^F+\Delta g_a^{F,T}\\ \Delta g_{v0}+\Delta g_v^F+\Delta g_v^{F,T}\\ \Delta g_{h0}+0+0\\ \Delta g_{r0}+0+0\end{bmatrix} \tag{57}$$

Where $[g_{01}{}^{\Delta,\ F,\ T},\ g_{02}{}^{\Delta,\ F,\ T},\ g_{03}{}^{\Delta,\ F,\ T},\ g_{04}{}^{\Delta,\ F,\ T}]^{\mathrm{T}}$ is the air gap model caused by thermoset coupling expansion, but the armature did not experience electromagnetic deflection.

In the modeling of temperature-induced air gap disturbances, according to the FEA, the change of the magnetic pole surface generated by the PMTM's thermo-solid coupling deformation is vertically symmetric. When the four initial air gaps are only vertically symmetrical (i.e., $g_{01}\neq g_{04}$ and $g_{02}\neq g_{03}$), the armature does not experience electromagnetic deflection. Additionally, there is no nonlinear interaction between the thermal-solid coupling deformation of the air gaps and magnetic properties. However, when the four initial air gaps are horizontally asymmetric (i.e., $g_{01}\neq g_{04}$ and $g_{02}\neq g_{03}$), the armature assembly experiences electromagnetic deflection due to unequal reluctance. The greater the horizontal asymmetry of the four air gaps, the greater the armature deflection angle. This results in a nonlinear interaction between thermal-solid coupling deformation and the magnetic properties of the four air gaps.

Zero-bias prediction model of PMTM

Based on the Z_{tm} of equation (35) and $Z_{\mathrm{tm}}{}^{T}$ of equation (36) in Section 3.1, the $[X_{g1}, X_{g2}, X_{g3}, X_{g4}]$ of equation (41) in Section 3.2, and the $[X_{g1}{}^{T}, X_{g2}{}^{T}, X_{g3}{}^{T}, X_{g4}{}^{T}]$ of equation (57) in Section 3.3, the specific expression of the zero-bias prediction model of PMTM can be derived directly.

Firstly, substituting the $[g_{01}{}^{\Delta,\ F},\ g_{02}{}^{\Delta,\ F},\ g_{03}{}^{\Delta,\ F},\ g_{04}{}^{\Delta,\ F}]$ of equation (35) into $T_{\mathrm{tm0}}(X_{g1}, X_{g2}, X_{g3}, X_{g4}, B_r)|_{Br\,=\,0.58\mathrm{T}}$, $K_t(X_{g1}, X_{g2}, X_{g3}, X_{g4}, B_r)|_{Br\,=\,0.58\mathrm{T}}$, $K_m(X_{g1}, X_{g2}, X_{g3}, X_{g4}, B_r)|_{Br\,=\,0.58\mathrm{T}}$ of the Appendix as well as neglecting the high-order terms, the T_{tm0} (unit: N•m), K_t (unit: N•m/A), and K_m (unit: N•m/rad) in equations (25)~(27) can be rewritten as

$$\begin{aligned}T_{\mathrm{tm0}}(X_{gi},B_r)&=T_{\mathrm{tm0}}^{\mathrm{n}}\cdot T_{\mathrm{tm0}}(X_{gi},B_r)|_{B_r=0.58\mathrm{T}}\\&=\left[1.65\times e^{-\frac{1}{2}\times\left(\frac{B_r-0.89358}{0.32873}\right)^2}-0.0529\right]\times\\&\quad\begin{bmatrix}-581\Delta g_{r0}+2.458\times10^6(\Delta g_{a0}\Delta g_{r0}+\Delta g_a^F\Delta g_{r0})\\+83.346\Delta g_{h0}+2.45\times10^6(\Delta g_{v0}\Delta g_{h0}+\Delta g_v^F\Delta g_{h0})\end{bmatrix}\end{aligned} \tag{58}$$

$$\begin{aligned}K_t(X_{gi},B_r)&=K_t^{\mathrm{n}}(B_r)\cdot K_t(X_{gi},B_r)|_{B_r=0.58\mathrm{T}}\\&=[1.73\times B_r+0.00425]\times[0.431-1.46\times10^3(\Delta g_{a0}+\Delta g_a^F)]\end{aligned} \tag{59}$$

$$\begin{aligned}K_m(X_{gi},B_r)&=K_m^{\mathrm{n}}(B_r)\cdot K_m(X_{gi},B_r)|_{B_r=0.58\mathrm{T}}\\&=\left[1.66\times e^{-\frac{1}{2}\times\left(\frac{B_r-0.89696}{0.32901}\right)^2}-0.0533\right]\times\\&\quad\begin{bmatrix}8.7+3.72\times10^4(\Delta g_{a0}+\Delta g_a^F)+\\3.335\times10^3(\Delta g_{v0}+\Delta g_v^F)\end{bmatrix}\end{aligned} \tag{60}$$

Similarly, when the temperature changes, substituting the $[g_{01}{}^{\Delta,\ F,\ T},\ g_{02}{}^{\Delta,\ F,\ T},\ g_{03}{}^{\Delta,\ F,\ T},\ g_{04}{}^{\Delta,\ F,\ T}.]^{\mathrm{T}}$ of equation (57) into the $T_{\mathrm{tm0}}(X_{g1}, X_{g2}, X_{g3}, X_{g4}, B_r)|_{Br\,=\,0.58\mathrm{T}}$, $K_t(X_{g1}, X_{g2}, X_{g3}, X_{g4}, B_r)|_{Br\,=\,0.58\mathrm{T}}$, $K_m(X_{g1}, X_{g2}, X_{g3}, X_{g4}, B_r)|_{Br\,=\,0.58\mathrm{T}}$ of the Appendix, as well as neglecting the high-order terms, the $T_{\mathrm{tm0}}{}^{T}$ (unit: N•m), $K_t{}^{T}$ (unit: N•m/A), and $K_m{}^{T}$ (unit: N•m/rad) in equation (33) can be rewritten as

$$\begin{aligned}T_{\mathrm{tm0}}^{T}(X_{gi}^{T},B_r^{T})&=T_{\mathrm{tm0}}^{\mathrm{n}}(B_r^{T})\cdot T_{\mathrm{tm0}}^{T}(X_{gi}^{T},B_r^{T})|_{B_r=0.58\mathrm{T}}\\&=\left[1.65\times e^{-\frac{1}{2}\times\left(\frac{B_r^T-0.89358}{0.32873}\right)^2}-0.0529\right]\times\\&\quad\begin{bmatrix}-581\Delta g_{r0}+2.458\times10^6\begin{pmatrix}\Delta g_{a0}\Delta g_{r0}+\Delta g_a^F\Delta g_{r0}\\+\Delta g_a^{F,T}\Delta g_{r0}\end{pmatrix}\\+83.346\times\Delta g_{h0}+2.45\times10^6\begin{pmatrix}\Delta g_{v0}\Delta g_{h0}+\Delta g_v^F\Delta g_{h0}\\+\Delta g_v^{F,T}\Delta g_{h0}\end{pmatrix}\end{bmatrix}\end{aligned} \tag{61}$$

$$\begin{aligned}K_t^{T}(X_{gi}^{T},B_r^{T})&=K_t^{\mathrm{n}}(B_r^{T})\cdot K_t^{T}(X_{gi}^{T},B_r^{T})|_{B_r=0.58\mathrm{T}}\\&=[1.73\times B_r^{T}+0.00425]\times[0.431-1.46\\&\quad\times10^3(\Delta g_{a0}+\Delta g_a^F+\Delta g_a^{F,T})]\end{aligned} \tag{62}$$

$$\begin{aligned}K_m^{T}(X_{gi}^{T},B_r^{T})&=K_m^{\mathrm{n}}(B_r^{T})\cdot K_m^{T}(X_{gi}^{T},B_r^{T})|_{B_r=0.58\mathrm{T}}\\&=\left[1.66\times e^{-\frac{1}{2}\times\left(\frac{B_r^T-0.89696}{0.32901}\right)^2}-0.0533\right]\times\\&\quad\begin{bmatrix}8.7+3.72\times10^4(\Delta g_{a0}+\Delta g_a^F+\Delta g_a^{F,T})\\+3.335\times10^3(\Delta g_{v0}+\Delta g_v^F+\Delta g_v^{F,T})\end{bmatrix}\end{aligned} \tag{63}$$

The zero-bias prediction model of PMTM Z_{tm} at room temperature and $Z_{\mathrm{tm}}{}^{T}$ at high temperature T can be precisely defined by replacing equations (58) and (59) into the Z_{tm} of equation (35) and equations (61) and (62) into the $Z_{\mathrm{tm}}{}^{T}$ of equation (36).

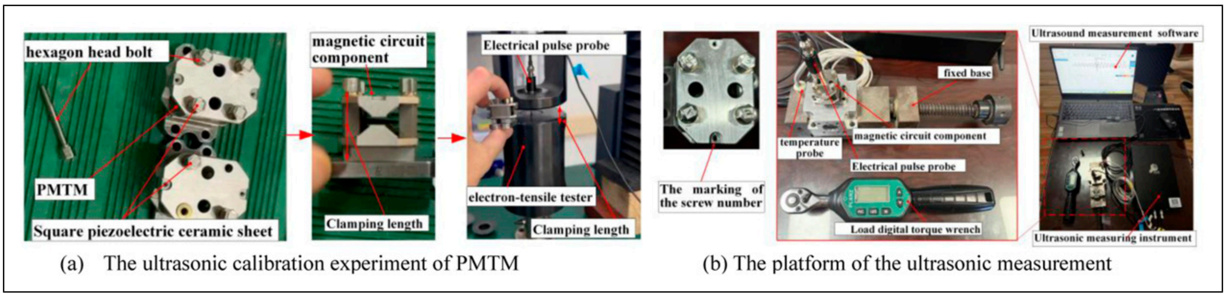

Figure 16. Ultrasonic calibration and measurement experiment of screw preload of PMTM.

$$Z_{\mathrm{tm}} = -\frac{T_{\mathrm{tm0}}(X_{gi},,B_{\mathrm{r}})}{K_{\mathrm{t}}(X_{gi},B_{\mathrm{r}})\cdot i_{\mathrm{rc}}}\times 100\% = -\frac{\left\{\begin{array}{l}\left[1.65\times e^{-\frac{1}{2}\times\left(\frac{B_{\mathrm{r}}-0.89358}{0.32873}\right)^2}-0.0529\right]\\ \times\left[\begin{array}{l}-581\Delta g_{\mathrm{r0}}+83.346\times\Delta g_{\mathrm{h0}}\\ +2.458\times 10^6\left(\Delta g_{\mathrm{a0}}\Delta g_{\mathrm{r0}}+\Delta g_{\mathrm{a}}^F\Delta g_{\mathrm{r0}}\right)\\ +2.45\times 10^6\left(\Delta g_{\mathrm{v0}}\Delta g_{\mathrm{h0}}+\Delta g_{\mathrm{v}}^F\Delta g_{\mathrm{h0}}\right)\end{array}\right]\end{array}\right\}}{\left\{\begin{array}{l}[1.73\times B_{\mathrm{r}}+0.00425]\times\\ \left[0.431-1.46\times 10^3\left(\Delta g_{\mathrm{a0}}+\Delta g_{\mathrm{a}}^F\right)\right]\end{array}\right\}\cdot i_{\mathrm{rc}}}\times 100\% \tag{64}$$

$$Z_{\mathrm{tm}}^T == -\frac{T_{\mathrm{tm0}}^T\left(X_{gi}^T,,B_{\mathrm{r}}^T\right)}{K_{\mathrm{t}}^T\left(X_{gi}^T,B_{\mathrm{r}}^T\right)\cdot i_{\mathrm{rc}}}\times 100\% - \frac{\left\{\begin{array}{l}\left[1.65\times e^{-\frac{1}{2}\times\left(\frac{B_{\mathrm{r}}^T-0.89358}{0.32873}\right)^2}-0.0529\right]\times\\ \left[\begin{array}{l}-581\Delta g_{\mathrm{r0}}+83.346\times\Delta g_{\mathrm{h0}}\\ +2.458\times 10^6\left(\begin{array}{l}\Delta g_{\mathrm{a0}}\Delta g_{\mathrm{r0}}+\Delta g_{\mathrm{a}}^F\Delta g_{\mathrm{r0}}\\ +\Delta g_{\mathrm{a}}^{F,T}\Delta g_{\mathrm{r0}}\end{array}\right)\\ +2.45\times 10^6\left(\begin{array}{l}\Delta g_{\mathrm{v0}}\Delta g_{\mathrm{h0}}+\Delta g_{\mathrm{v}}^F\Delta g_{\mathrm{h0}}\\ +\Delta g_{\mathrm{v}}^{F,T}\Delta g_{\mathrm{h0}}\end{array}\right)\end{array}\right]\end{array}\right\}}{\left\{\begin{array}{l}[1.72631\times B_{\mathrm{r}}^T+0.004255]\times\\ \left[0.431-1.46\times 10^3\left(\Delta g_{\mathrm{a0}}+\Delta g_{\mathrm{a}}^F+\Delta g_{\mathrm{a}}^{F,T}\right)\right]\end{array}\right\}\cdot i_{\mathrm{rc}}}\times 100\% \tag{65}$$

Finally, the thermal drift of zero-bias for PMTM $\Delta Z_{\mathrm{tm}}{}^T$ at temperature T can be given as

$$\Delta Z_{\mathrm{tm}}^T = Z_{\mathrm{tm}}^T - Z_{\mathrm{tm}} \tag{66}$$

Experimental verification

This section tests the validity of the aforementioned model using three experiments. First, the pre-tightening force of the screw in the PMTM is measured using ultrasonic technology, and the results are compared to those from the ABAQUS. Following that, the experimental results of the length of the air gap, as well as the zero-bias current, are compared to those predicted by the theoretical model, using an image size measurement device and the zero-bias testing bench. Finally, a testing apparatus is developed for evaluating the PMTM's displacement at high temperatures. The output displacement of the feedback rod ball at temperatures of 30°C and 180°C is measured and compared to that predicted by a physical model.

Experimental study of the pre-tightening force

Ultrasonic technology works by sending and receiving electrical signals to a piezoelectric ceramic sheet positioned at the head of a screw. The time difference between the electrical signals emitted and received during the screw's free and tightened states is measured. This time difference determines the screw's elongation deformation. The pre-tightening force is then computed using the material's elastic modulus, screw cross-sectional area, and Hooke's law. Figure 16 depicts the ultrasonic calibration and measurement experiment of screw preload of PMTM, and the result of the calibration coefficient is 0.03163.

The calibration coefficient is entered into the host of an ultrasonic measurement instrument in Figure 16(b). The electronic tensile testing machine is loaded at random, and the results of the screw's axial force as measured by the ultrasonic measuring instrument and the tensile testing machine are observed and recorded simultaneously, as shown in Table 2. It can be shown that the calibration

Table 2. The accuracy of the calibration coefficient.

Value of testing machine/kN	0.61	1.22	1.94	2.26
Value of ultrasonic system/kN	0.62	1.24	1.96	2.27
The error of comparison/%	1.63	1.64	1.03	0.4

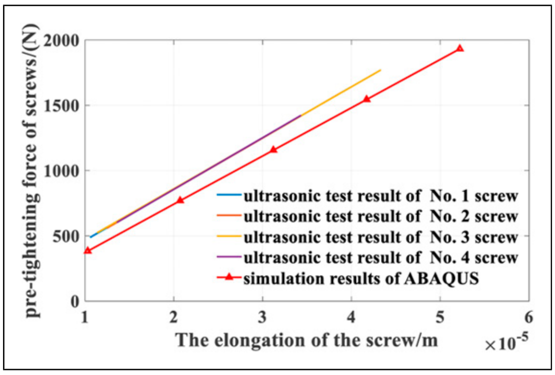

Figure 17. Comparison of test and simulation results.

findings have a test error of less than 2%, indicating that they are highly accurate and can be utilized in the following pre-tightening studies.

As shown in Figure 17, the average value of the ultrasonic measurement results of the stiffness of four screws and the simulation results are 3.9185e7 and 3.6956e7, respectively, with a relative error of 5.6%, indicating that the established ABAQUS model of pre-tightening force is relatively accurate.

Experimental study of air gap length and zero-bias for PMTM at room temperature

The four initial air-gap lengths (Δg_{0i}^{Δ}, i = 1~4) and the interference fit value of armature δ_{int} are assumed to follow a normal distribution within their distribution range. If $\Delta g_{0i}^{\Delta} \le Err\_\Delta g_{0i}^{\Delta}$ (i = 1~4) and $\delta_{\text{int}} \le Err\_\delta_{\text{int}}$, we can have $\Delta g_{0i}^{\Delta} \sim N(0, (Err\_\Delta g_{0i}^{\Delta}/6)^2)$ and $\delta_{\text{int}} \sim N(0, (Err\_\delta_{\text{int}}/6)^2)$. Figure 18 depicts the flow chart for air-gap sample production and zero-bias computation for batch PMTMs. We can obtain theoretical results for the distribution characteristics of the zero-bias and air gap of batch PMTMs at room temperature, which are then compared to the experimental data. The theoretical model has an initial value of n = 100, $Err\_\Delta g_{0i}^{\Delta}$ = 40 μm, Err_δ_{int} = 5 μm, $Err\_g_{\text{h}} = Err\_g_{\text{v}}$ = 100 μm, T = 20°C, F_{ms0} = 2200N, and B_{r} = 0.58 T.

As shown in Figure 19, an image-size measuring equipment extracts the lengths of the upper and lower air gaps, while the static characteristic curve extracts the zero bias current. The frequency distribution histograms of the lengths of four air gaps and zero-bias of 10 PMTMs are obtained and compared with the theoretical results obtained by the $g_{01}^{\Delta,F,Br} \sim g_{04}^{\Delta,F,Br}$ in equation (46) and the Z_{tm} in equation (64). As shown in Figures 20 and 21, respectively. The distribution of air gap and zero-bias of batch PMTMs produced by the test exhibits a certain fluctuation under the perturbation of the manufacturing process parameters, which is in line with the theoretical model's overall forecast trend. Additionally, Table 3 lists the theoretical and experimental values of the zero-bias distribution characteristic parameters and the air gap distribution range. It is evident that the test's distribution range of the air gap is essentially in line with the simulation's findings. There is a certain difference between the experimental and theoretical values for the zero-bias distribution characteristic parameters, but they are all of the same magnitude.

The difference between the test and theoretical values can be attributed to two major factors. On the one hand, due to test condition limitations, there is still a certain difference between the number of PMTMs assessed by the zero-bias test and the number of PMTMs whose distribution characteristic parameters converge to a constant value. On the other hand, the influence of the release of

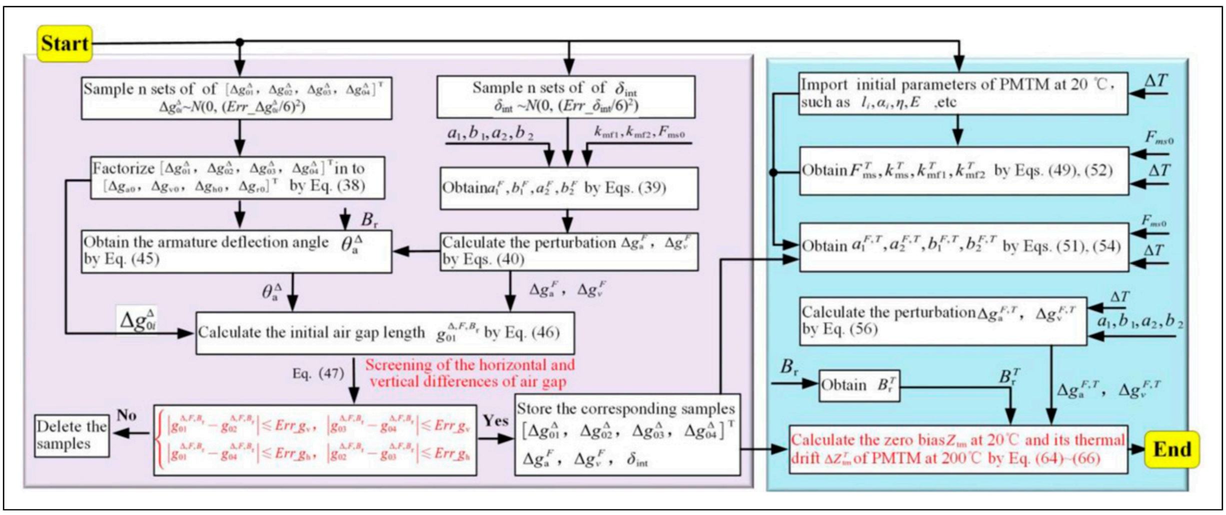

Figure 18. Flow chart of sample generation of air-gap and calculation of zero-bias and its thermal drift for batch PMTM.

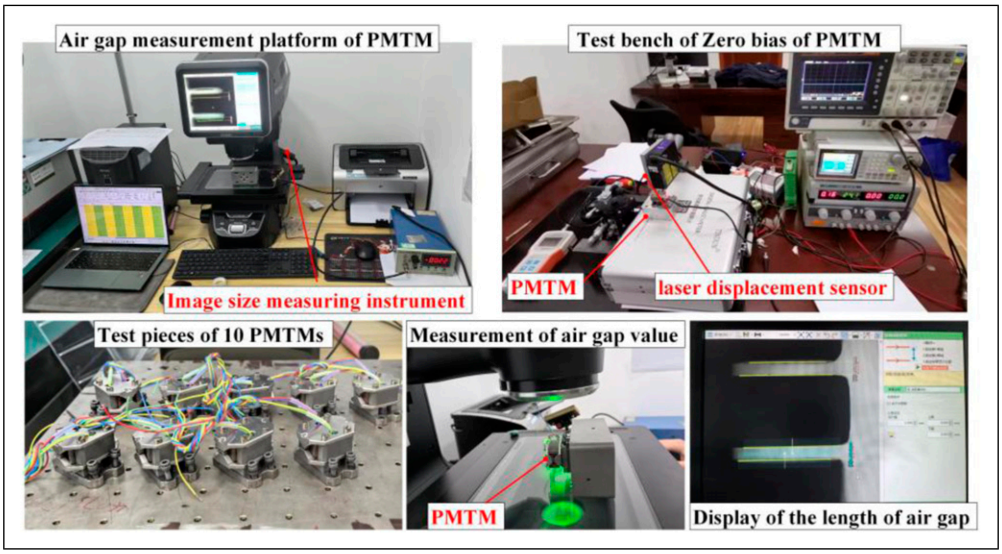

Figure 19. The comparison between the theoretical and experimental values of the lengths of the air gap of batch PMTMs.

assembly stress and creep on the air gap length is not considered in the theoretical model, resulting in a certain gap in the results.

Experimental study of output characteristics of PMTM under high temperature

A new high-temperature testing system for PMTM is created, as shown in Figure 22(a), and a physical prototype is built, as shown in Figure 22(b). The high-temperature environment simulation system consists primarily of a thermostat, a relay, a ceramic heater, a left (right) insulating pad, a fixed bracket, a thermocouple, a thermometer, and so on. The left thermal insulation pad, the ceramic heater, and the right thermal insulation pad form a heating and insulation chamber that is utilized to provide a high-temperature operating environment for the PMTM. The PMTM is secured to the right fixation bracket using a first-stage seat screw. High-temperature-resistant sealing tape is used to connect the heater and the heat insulation pad, preventing internal heat from leaking from the heating and insulation chamber.

The conventional method for temperature control accuracy and heating uniformity is as follows: The temperature controller is used to adjust the heating temperature, which controls the relay's contact action, turning on and off the ceramic heater. Four thermocouples (thermocouple 1 ~ 4) are attached to various areas of the PMTM's exterior surface. One of the thermocouple signals is given back to the thermostat, allowing for closed-loop modification of the PMTM's heating temperature. The remaining three thermocouple signals can be linked to the thermometer to see the PMTM's temperature distribution.

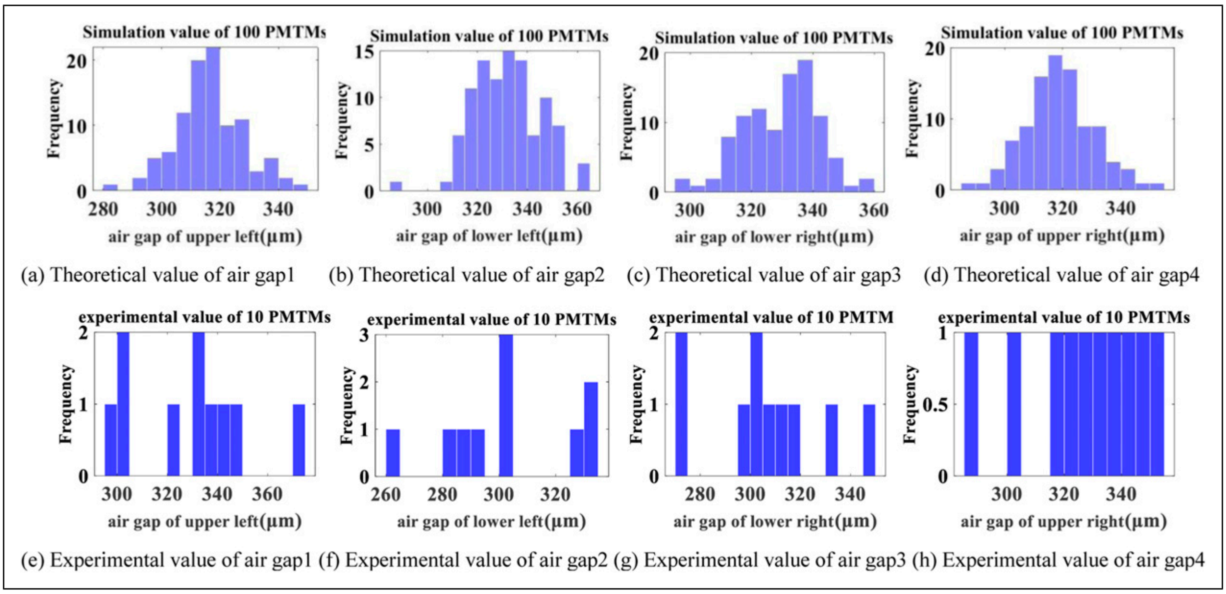

Figure 20. The comparison between the theoretical and experimental values of the lengths of four air gaps of batch PMTMs.

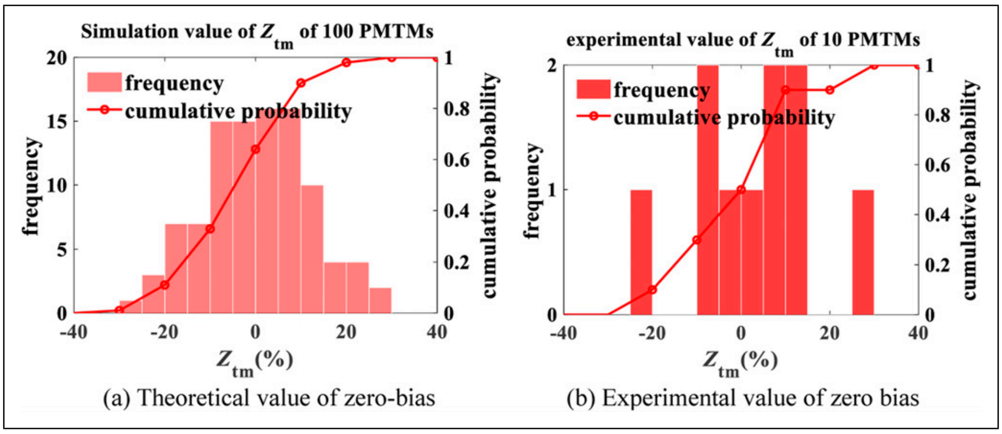

Figure 21. The comparison between the theoretical and experimental values of the zero-bias for batch PMTMs.

During the test, thermocouple probes 1–4 are attached to the center of the outer surface of the vertical section of the lower magnetizer, the center of the outer surface of the horizontal section of the upper magnetizer, the center of the outer surface of magnet steel 1, and the center of the outer surface of magnet steel 2. The temperature of the magnetic steel detected by thermocouple 3 is utilized as an output signal to access the temperature controller, which adjusts the temperature in a closed loop. The remaining three thermocouples are attached to the thermometer in sequence to view and record the temperature. The sampling period is set at 10 s.

Figure 23 shows the time-temperature curve of the exterior surface of permanent magnet 2 at a temperature of 50°C. The thermometer recorded temperature data for 116 min, with a 10-s sampling period. After heating PMTM from room temperature for 116 min, the recorded temperature stabilizes between 50°C and 52°C. The actual measured temperature is 18.7°C. At this moment, the temperature distribution in the PMTM is thought to have reached a stable condition. The controller's on/off control method results in an overshoot of approximately 16.5% in the curve. To prevent damage to the PMTM from high temperatures, a maximum heating temperature of 180°C is set.

Figure 24 shows the steady-state temperature readings of the upper yoke, lower yoke, permanent magnet 1, and permanent magnet 2 at various preset settings (T_{preset} = 50°C, 80°C, 120°C, 150°C). The bottom yoke has the lowest temperature because of heat transfer factors. The range R_T of the measured temperature distribution of PMTM expands as the preset temperature increases. At preset temperatures of 50°C, 80°C, 120°C, and 180°C, the range of R_T is 2.3°C, 6.2°C, 7.4°C, and 11.3°C, with corresponding relative values of 4.6%, 8.1%, 6.1%, and 6.2%, respectively. This illustrates how well the heating and insulation subsystem provides an effective high-temperature environment for the PMTM's static characteristic measurement.

Figure 25 shows the theoretical and experimental findings of the output displacement of the feedback rod ball at temperatures of 30°C and 180°C. The PMTM's measured initial air-gap lengths are 342.4 μm, 316.2 μm, 320.5 μm, and 348.1 μm for g_{01}, g_{02}, g_{03}, and g_{04}. Based on the original data, we also provide the real-time comparison error of 30°C and 180°C. The average relative errors of the feedback ball's output displacement at 30°C and 180°C are 5.16% and 6.66%, respectively. The largest relative error between theoretical and experimental values is 10.6% and 10.7%, respectively. This demonstrates the high degree of consistency between theoretical and experimental outcomes.

Discussion

The zero-bias mechanism of PMTM

Figure 26 depicts a schematic diagram of the PMTM with and without zero bias. As shown in Figure 26(a), if the machining error of the magnetic pole surface leads to the horizontal asymmetry of the four initial air gaps of the torque motor, that is, $g_{01} \neq g_{04}$ and $g_{02} \neq g_{03}$, the screw connection leads to the downward movement of the magnetic pole surface of the magnetizer, and the

Table 3. Distribution range of air gap and distribution characteristic parameters of zero-bias of batch PMTMs.

	The range of air gap distribution/(μm)	The distribution mean of Z_{tm} of batch PMTMs(%)	The distribution variance of Z_{tm} of batch PMTMs(%^{2})
Theoretical value(100 PMTMs)	280∼360	9.44	48.21
Experiment value (10 PMTMs)	260∼380	11.01	66.35

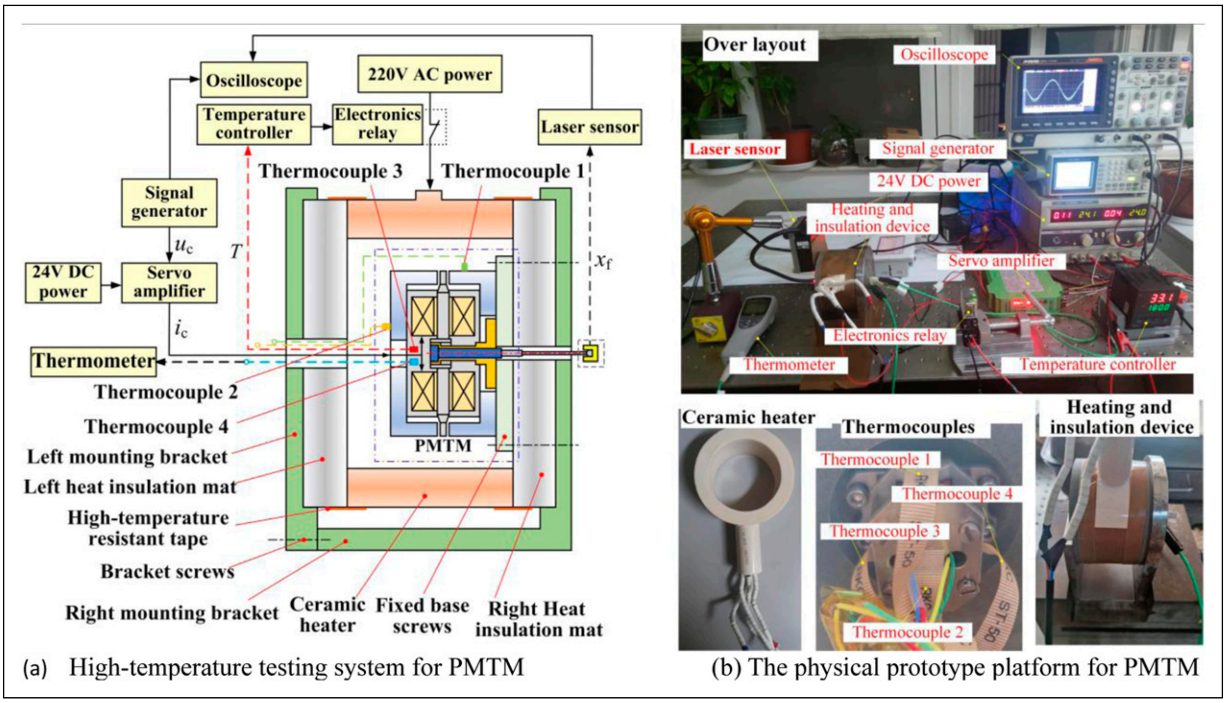

Figure 22. Schematic diagram of the high-temperature testing system of PMTM.

interference fit leads to the arc deformation of the armature magnetic pole surface. The interaction between the two will inevitably aggravate or weaken the horizontal symmetry of the initial air gap. Then, the magnetization of the magnetic steel causes the armature assemblies to deflect under the action of the electromagnetic force, and the PMTM generates a zero bias. As shown in Figure 26(b), if the magnetic pole surface machining error causes the four initial air gaps of the PMTM to be horizontally symmetrical, that is, $g_{01} = g_{04}$ and $g_{02} = g_{03}$, although the screw connection and interference fit cause the magnetic pole surface to move, the four air gaps are still horizontally symmetrical, which essentially does not cause the armature assemblies to deflect, and the PMTM will not produce zero-bias.

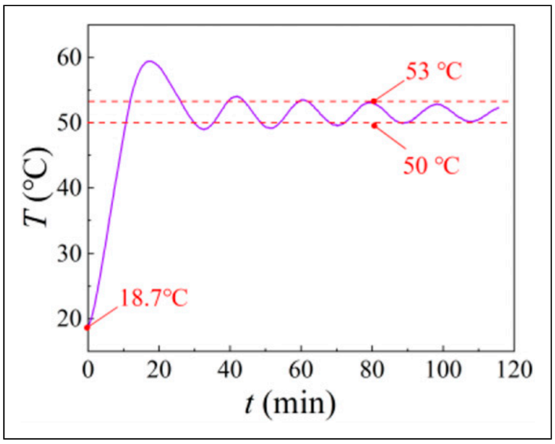

Figure 23. Temperature curve at the outside surface of magnet 2.

Furthermore, high temperatures degrade magnetic characteristics and result in the thermo-solid coupling deformation of magnetic circuit and armature assemblies, respectively. Based on the above-mentioned verified model, the influence weights of the three elements' cross-coupling on the distribution features of thermal drift of zero-bias for batch PMTMs are quantitatively studied. The three factors are the thermo-solid coupling deformation of the magnetic circuit assemblies ($a_1^{F,\ T}$ and $a_2^{F,\ T}$), the thermo-solid coupling deformation of the armature assemblies ($b_1^{F,\ T}$ and $b_2^{F,\ T}$), and the temperature change in the remanent magnetism (B_r^{T}).

We examined the distribution characteristics of the thermal drift of zero-bias for batch PMTMs under the following cases by substituting the following values into Figure 18: samples n = 1000, the control range of processing error of magnetic pole surface for yoke and armature $Err\_\Delta g_{0i}^{\Delta}$ = 40 μm, the pre-tightening force F_{ms0} = 2200N, the remanent magnetism B_r = 0.58 T, the

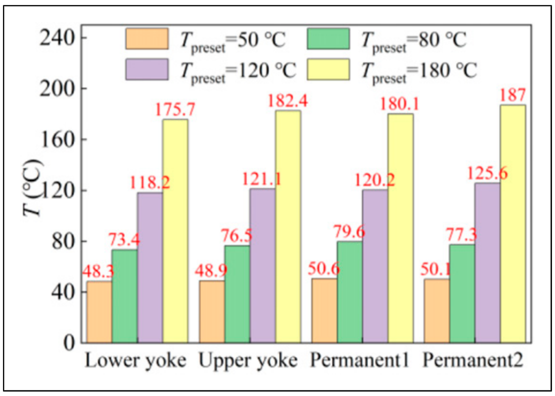

Figure 24. Temperature distribution of PMTM.

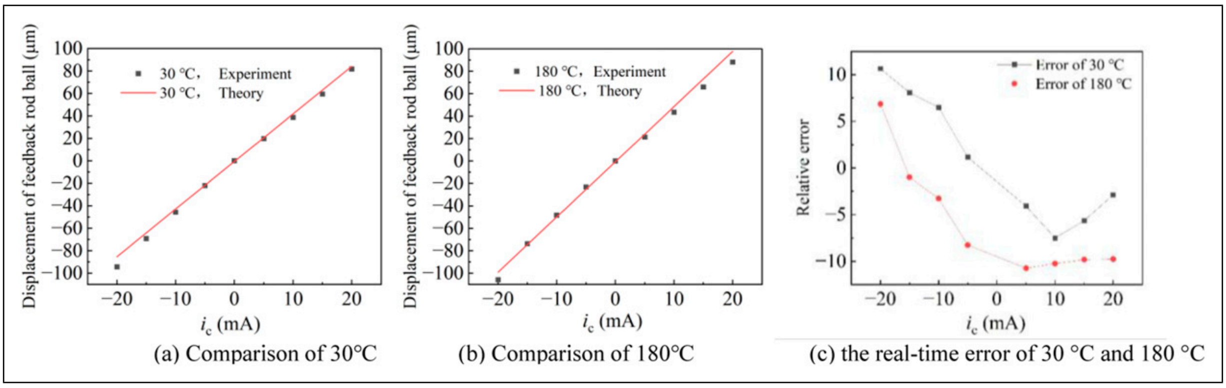

Figure 25. Theoretical and experimental results of the output displacement of the feedback rod ball at 30°C and 180°C.

interference amount at armature $Err\_\delta_{int} = 5$ μm, the control range of difference on horizontal and vertical of air gap $Err\_g_h = Err\_g_v = 20$ μm, and temperature $T = 200$°C. We can obtain 235 sets of X_{gi} and thermal drift of zero-bias $\Delta Z\,T$ tm under the above cases since $Err\_g_h = Err\_g_v = 20$ μm, as shown in Figure 27. These six cases are as follows:

(a) Case 1: Only considering $a_1^{F,\ T}$, and $a_2^{F,T}$; neglecting the temperature effect of b_1^{F}, b_2^{F}, and B_r;
(b) Case 2: Only considering $b_1^{F,\ T}$, and $b_2^{F,T}$; neglecting the temperature effect of a_1^{F}, a_2^{F}, and B_r;
(c) Case 3: Considering both $a_1^{F,T}$, and $a_2^{F,\ T}$, and $b_1^{F,\ T}$ and $b_2^{F,\ T}$; neglecting the temperature effect of B_r;
(d) Case 4: Considering both $a_1^{F,\ T}$, $a_2^{F,\ T}$, and B_r^{T}; neglecting the temperature effect of $b_1^{F,\ T}$, and $b_2^{F,T}$;
(e) Case 5: Considering both $a_1^{F,T}$, $a_2^{F,\ T}$, and B_r^{T}; neglecting the temperature effect of $a_1^{F,\ T}$, and $a_2^{F,T}$;
(f) Case 6: Considering $a_1^{F,T}$, $a_2^{F,\ T}$, $b_1^{F,\ T}$, $b_2^{F,T}$, and B_r^{T}.

To assess the impact of various factors on the thermal drift of zero-bias for batch PMTMs, a quantitative evaluation standard ($EC_{\Delta Z}$) is used, which can be represented as

$$EC_{\Delta Z}(i)|_{i=1\sim5} = \frac{\sum_{j=1}^{n} \left|\Delta Z_{tm}^{200^{\circ}C}(i,j) - \Delta Z_{tm}^{200^{\circ}C}(6,j)\right|}{n(n=235)} \tag{67}$$

Where $EC_{\Delta Z}$ are the indicators for evaluating the degrees of influence exerted by the factors on the thermal stability of zero-bias, i represents the number of cases; j represents the number of samples of PMTMs.

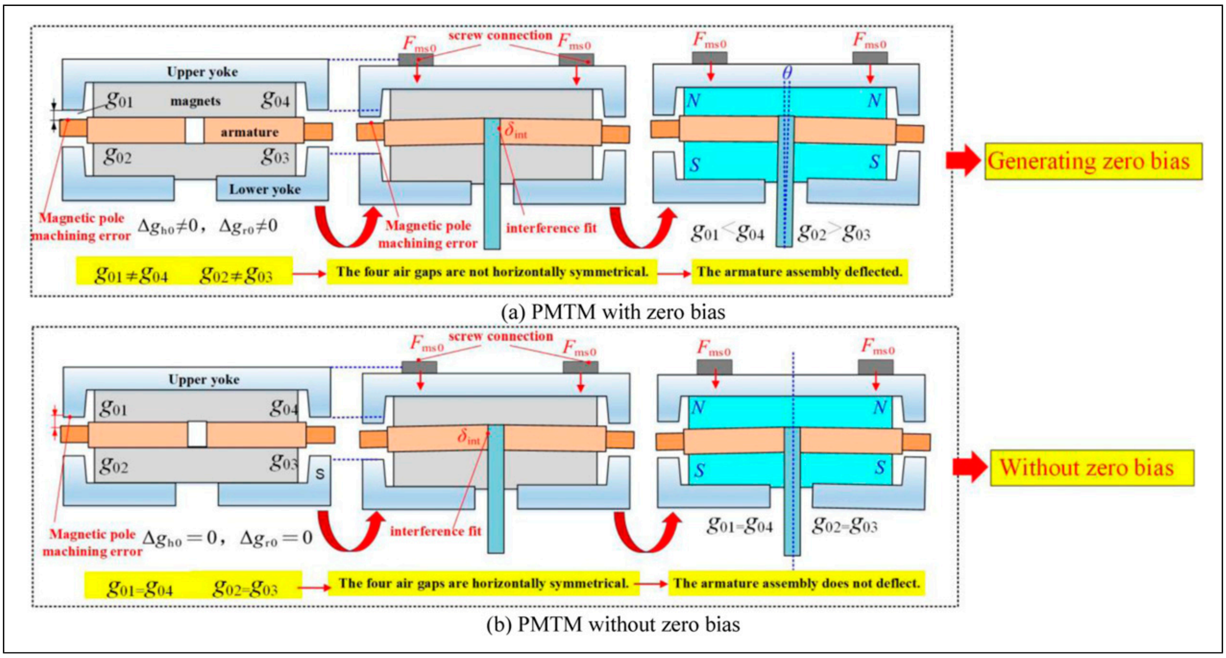

Figure 26. The principal diagram of zero bias of PMTM.

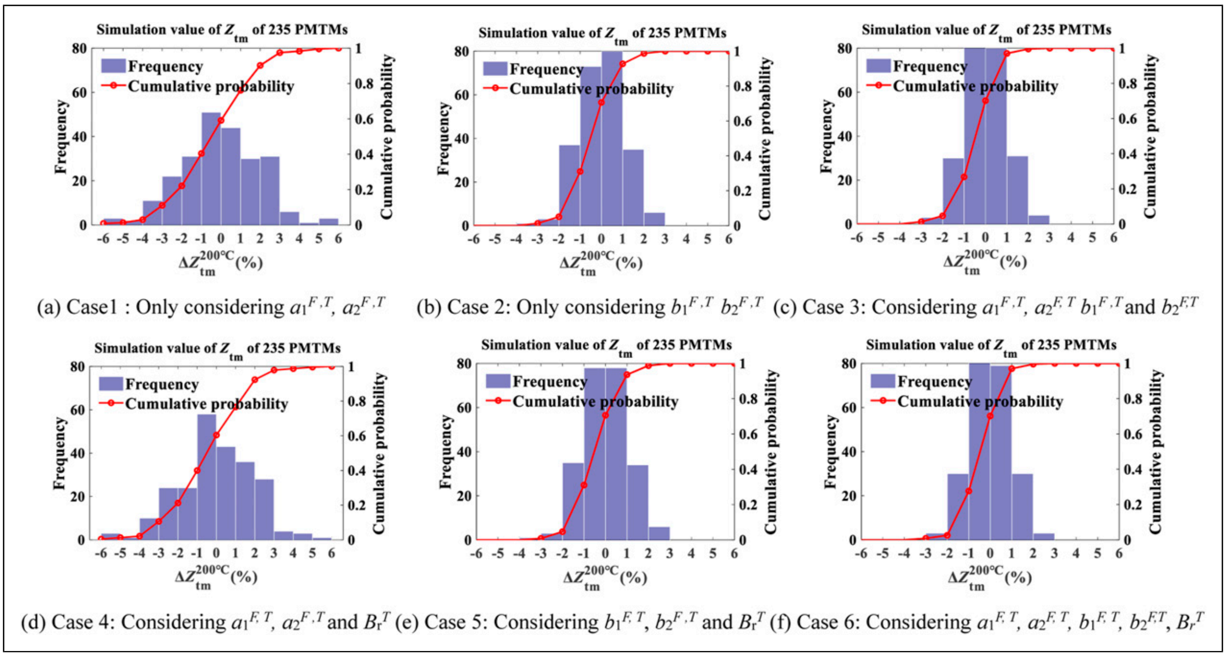

Figure 27. Distribution mean of the thermal drift of zero-bias $\Delta Z_{tm}{}^{T}$ for 235 PMTMs under different cases.

Substituting the computation results of (a)~(e) of Figure 27 into the above equation (67), the $EC_{\Delta Z}$ of cases 1~5 can be obtained, as listed in the Table 4.

From Table 4, it is clear that, of all the important design factors of PMTM, the thermo-solid coupling deformation of the armature assemblies ($b_1^{F,\ T}$ and $b_2^{F,\ T}$) has the greatest influence on the thermal drift of zero bias.

Figure 28 shows the distribution mean of zero-bias Z_{tm} at 20°C and the distribution mean of thermal drift of zero-bias $\Delta Z_{tm}{}^{200°C}$ at 200°C for batch PMTMs under the impact of four varying process parameters, Err_g_v, Err_g_h, F_{ms0}, and B_r. In particular, as shown in Figure 28(a) and (b), the $\mu(Z_{tm})$ increases from 0.71% to 4.04% and from 0.77% to 2.64% as Err_g_v and Err_g_h increase from 5 μm to 50 μm, respectively. This indicates that the zero-bias Z_{tm} of PMTM at 20°C is more sensitive to the change of vertical difference of air gap Err_g_v than the difference of horizontal difference Err_g_h. Furthermore, as shown in Figure 28(b) and (c), the $\mu(Z_{tm})$ decreases as the pre-tightening force F_{ms0} and remanent magnetism B_r rise. The above results indicate that the zero-bias Z_{tm} at 20°C can be effectively suppressed by prioritizing control of the error limit of vertical difference of air gap, increasing pre-tightening force, and remanent magnetism. The distribution mean of thermal drift of zero-bias $\Delta Z\ T$ tm of batch PMTMs at 200°C is nearly steady within 1% and unaffected by the four process parameters listed above.

Table 4. Quantitative evaluation indicators obtained in Cases 1~5.

Case *i*	$EC_{\Delta Z}$ (%)
Case 1	0.8635
Case 2	0.1096
Case 3	0.0354
Case 4	0.8099
Case 5	0.0920

Limitation analysis of this work

(1) This paper focuses on the displacement features of the feedback rod ball under ambient temperature action using the external uniform heating method. However, the temperature in the flight environment is typically 200°C, whereas internal fluid temperatures are about 140°C. The interaction between the two may cause the highest temperature in the middle of the feedback rod, resulting in a thermal deformation trend that is contrary to the external environment's heating direction, which may not fully replicate the genuine condition. The findings of this study are most directly applicable in explaining the thermal effects induced by the external environment or uniform heat load. In the future, we may conduct additional internal fluid thermal coupling tests to better forecast the PMTM's performance after the actual heat transfer balance.

(2) When using the laser displacement sensor for high-temperature in situ measurement at 180°C, the laser beam must travel through a non-uniform temperature field around the measured object (the feedback rod ball). The laser emitted by the sensor must pass through the hot air layer created by self-heating (180°C) above the feedback rod ball. Because there is a large temperature and density differential between this layer and the surrounding room temperature air, beam deflection could be a source of measurement inaccuracies. To eliminate

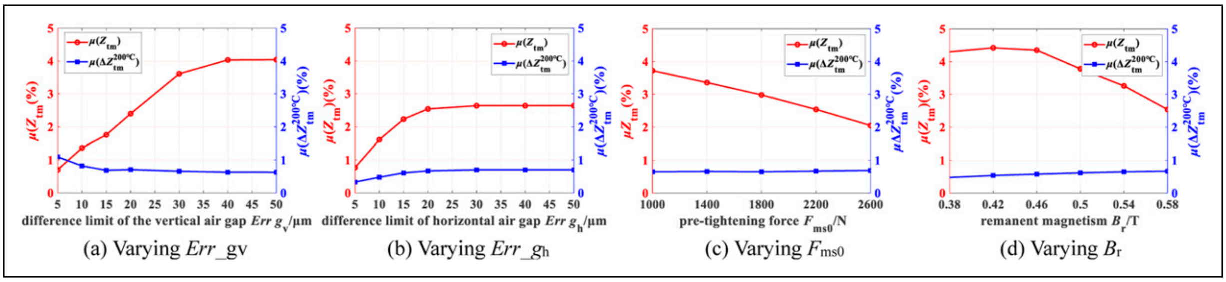

Figure 28. Distribution mean of zero-bias for batch PMTMs under the impact of four varying process parameters, Err_g_v, Err_g_h, F_{ms0}, and B_r.

this impact and obtain greater precision in absolute measurement, future studies will lower the length of the measuring optical path in the high-temperature zone as much as feasible, as well as the path of refractive index integration.

(3) Due to experimental cost and time constraints, this study originally analyzed statistical trends using 10 experimental samples. Despite the restricted sample size, the results can highlight the basic distribution trend and magnitude of PMTM essential parameters, as well as give preliminary experimental verification for the simulation model. Future research will incorporate bigger experimental samples to allow for more robust statistical inference.

Conclusions

(1) Response surface methods and finite element analysis are combined to provide a zero-bias predictive model of PMTM. The model takes into account a number of elements, such as machining errors on magnetic pole surfaces, interference and screw connections, armature electromagnetic deflection, and temperature impacts on structural deformation and magnetic characteristics.

(2) In the experiment at room temperature, the test results for the distribution range of air gaps for batch PMTMs are largely compatible with the theoretical findings. The experimental and calculated values for zero-bias distribution characteristic parameters are all of the same order of magnitude.

(3) In the experiment of high temperature, at preset temperatures of 50°C, 80°C, 120°C, and 180°C, the R_T range is 2.3°C, 6.2°C, 7.4°C, and 11.3°C, with corresponding relative values of 4.6%, 8.1%, 6.1%, and 6.2%. This indicates the efficiency of the heating and insulation subsystem in providing a consistent high-temperature environment for PMTM. The greatest relative errors between theoretical and actual values for feedback rod ball displacement at 30°C and 180°C were 10.6% and 10.7%, respectively.

(4) The thermo-solid coupling deformation of the armature assemblies has the greatest impact on the thermal drift of zero-bias for PMTM. At room temperature, the zero-bias is more sensitive to changes in the vertical difference in air gap than the horizontal difference. The zero-bias of PMTM at room temperature can be efficiently controlled by prioritizing control over the error limit of the vertical difference of the air gap.

ORCID iDs

Leilei Niu https://orcid.org/0009-0000-1659-9757
Yuchuan Zhu https://orcid.org/0000-0002-7399-1656

Funding

The authors disclosed receipt of the following financial support for the research, authorship, and/or publication of this article: This work was supported by the National Natural Science Foundation of China (Grant No. 52375059).

Declaration of conflicting interests

The authors declare that there is no conflict of interest.

References

1. Ge SH, Yang HH, Cheng WH, et al. Mathematical modeling and experimental investigation of pressure characteristics inside the pilot stage of the deflector jet servo-valve considering secondary jet velocity distribution. *Proc Inst Mech Eng G J Aerosp Eng* 2024; 238(16): 1624–1637. https://doi.org/10.1177/09544100241277234
2. Gao JF, Shi YQ, Xu YP, et al. Principle and pressure loss experiment of electro-hydraulic slide-rotary direction valve in single-pump and multi-motor hydraulic system. *Adv Mech Eng* 2024; 16(10): 11. https://doi.org/10.1177/16878132241284346
3. Ding YL, Liu YH, Luo YF, et al. Du, heat transfer analysis for servo valve in hydraulic servo actuator of aero engine vectoring nozzle. In: *2016 52nd AIAA/SAE/ASEE joint propulsion conference; July 25-27*. American Institute of Aeronautics and Astronautics, 2016.
4. Cai CP, Peng YR, Zheng QG, et al. Vector deflection stability control of aero-engine based on linear active disturbance rejection. *Chin J Aeronaut* 2022; 35(8): 221–235. https://doi.org/10.1016/j.cja.2021.11.011
5. Li Y and Wang ZH. Aero-engine guide vane angle regulator iterative learning control method. In: *2018 IEEE 3rd*

advanced information technology, electronic and automation control conference (IAEAC); October 12-14. IEEE Press, 2018, pp. 2401–2405.
6. Hang J, Li YH and Yang LM. A novel low-pressure-difference fluctuation electro-hydraulic large flowrate control valve for fuel flowrate control of an aeroengine afterburner system. *Chin J Aeronaut* 2022; 35(11): 363–376. https://doi.org/10.1016/j.cja.2021.07.002
7. Yuan Y, Zhang TH, Lin ZL, et al. An investigation into factors determining the metering performance of a fuel control unit in an aero engine. *Flow Meas Instrum* 2020; 71(71): 101672. https://doi.org/10.1016/j.flowmeasinst.2019.101672
8. Gan YF, Liao SY, Wu TY, et al. Analysis of the influence of expansion gap on thermal stress and strain distribution of a hot blast stove. *Adv Mech Eng* 2024; 16(10): 16. https://doi.org/10.1177/16878132241286196
9. Yao JY and Liu HJ. Quality prediction for rocket body structure manufacturing process based on improved ELM. *Adv Mech Eng* 2024; 16(10): 10. https://doi.org/10.1177/16878132241289758
10. Merritt EH. *Hydraulic control systems*. John Wiley & Sons, Inc., 1967, pp. 133–144.
11. Urata E. On the torque generated in a servo valve torque motor using permanent magnets. *Proc Inst Mech Eng C-J Mech Eng Sci* 2007; 22(5): 519–525. https://doi.org/10.1243/0954406jmes584
12. Liu CH and Jiang HZ. Influence of magnetic reluctances of magnetic elements on servo valve torque motors. *Chin J Mech Eng* 2016; 29(1): 136–144. https://doi.org/10.3901/cjme.2015.1204.142
13. Zhang QF, Yan L, Duan ZH, et al. High torque density torque motor with hybrid magnetization pole arrays for jet pipe servo valve. *IEEE Trans Ind Electron* 2019; 67(3): 2133–2142. https://doi.org/10.1109/tie.2019.2903761
14. Urata E. Influence of fringing on servo valve torque-motor characteristic. *Proc JFPS Int Symp Fluid Power* 2002; 2002: 769–774. https://doi.org/10.5739/isfp.2002.769
15. Urata E. One-degree-of-freedom model for torque-motor dynamics. *Int J Fluid Power* 2004; 5(2): 35–42. https://doi.org/10.1080/14399776.2004.10781190
16. Urata E. Influence of unequal air-gap thickness in servo valve torque motors. *Proc Inst Mech Eng C-J Mech Eng Sci* 2007; 221(11): 1287–1297. https://doi.org/10.1243/09544062jmes709
17. Chen ZC, Ge SH, Jiang YL, et al. Refined modeling and experimental verification of a torque motor for an electro-hydraulic servo valve. *Chin J Aeronaut* 2023; 36(6): 302–317. https://doi.org/10.1016/j.cja.2023.01.014
18. Zhang Y, Wang SP, Shi J, et al. Evaluation of thermal effects on temperature sensitive operating force of flow servo valve for fuel metering unit. *Chin J Aeronaut* 2020; 33(6): 1812–1823. https://doi.org/10.1016/j.cja.2019.09.011
19. Yan H, Liu Y and Ma L. Mechanism of temperature's acting on electro-hydraulic servo valve. *IEEE Access* 2019; 7(7): 80465. https://doi.org/10.1109/access.2019.2922135
20. Kang J, Yuan Z and Li J. Mechanism analysis and evaluation of thermal effects on the operating point drift of servo valves. *J Zhejiang Univ-Sc A* 2022; 23(4): 286–302. https://doi.org/10.1631/jzus.a2100464
21. Ma L, Yan H, Cai CK, et al. Temperature drift mechanism of deflector jet servo valve under temperature shock. *AIP Adv* 2023; 11(6): 065210.
22. Liu X, Yin YB, Zheng W, et al. The modeling and analysis of operating characteristics and temperature drift of deflector jet servo valve under a wide temperature range. *Proc Inst Mech Eng C-J Mech Eng Sci* 2024; 238(12): 5921–5936.
23. Jiang YL, Zhu YC, Ge SH, et al. Effect of screw assembly stress and stress relaxation on electrohydraulic pressure servo valve's zero position. *J Nanjing Univ Aeronaut Astronaut* 2021; 453(03): 350–358.
24. Yin YB, Li C, Li CM, et al. Influence of torque motor air-gap error on electro-hydraulic servo valve zero deviation. *J. Huazhong Univ. of Sci.& Tech(Natural Science Edition)* 2019; 47(03): 55–61.
25. Xia T, Chen Y and Zhang J. Influence of stress asymmetry and thermal deformation on zero position of jet pipe servo valve at high temperature. *Chin Hydraul Pneum* 2023; 47(08): 155–166.

Appendix

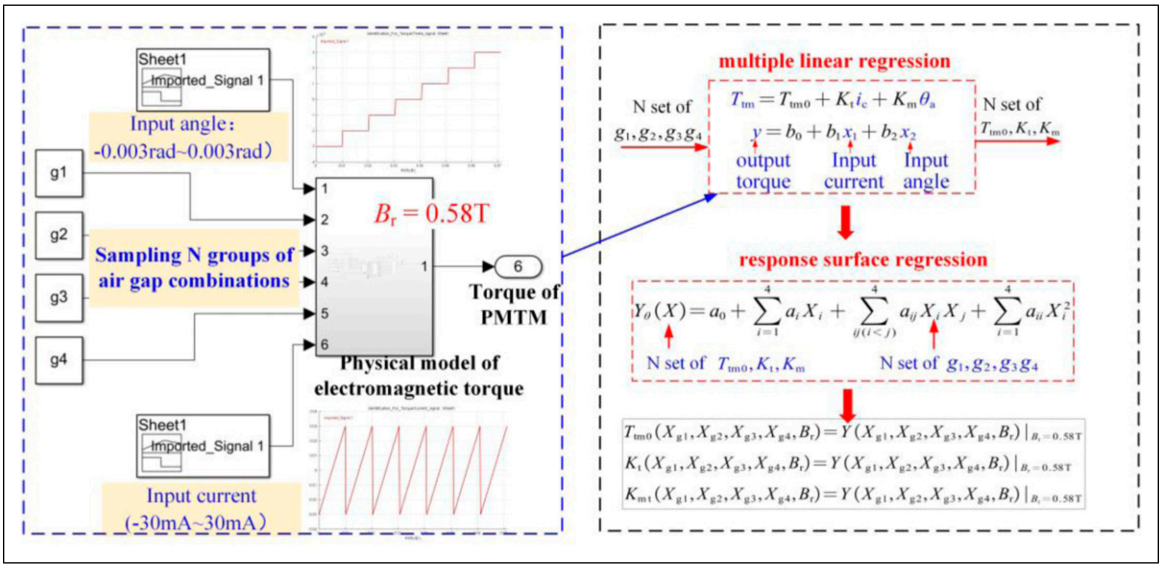

Figure A.1. Identification principle of the surrogate model of electromagnetic torque for PMTM.

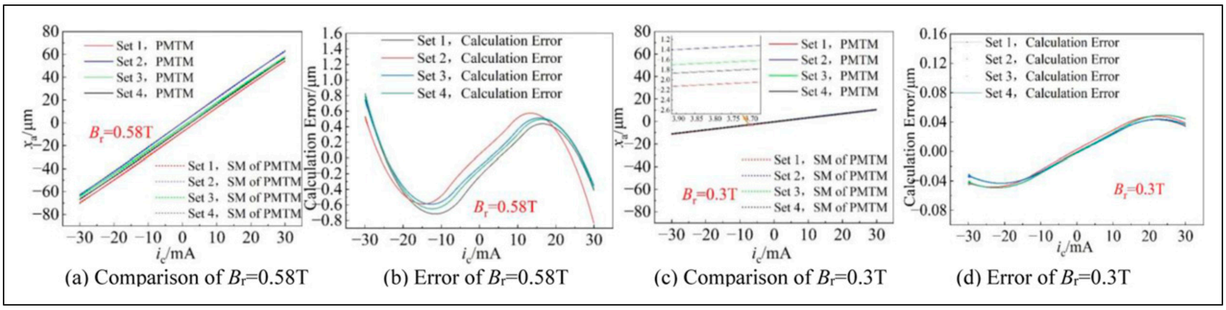

Figure A.2. Prediction accuracy of the third-order response surface surrogate model and the physical model.

Table A.1. Physical-mechanical parameters of each part for PMTM under T = 20~200°C.

Parts	Material	Density (g/cm^3)	Young's modulus at T = 20°C (Gpa)	Temperature coefficient of Young's modulus η (10^{-5}/°C)	Poisson's ratio	Linear thermal expansion coefficient α (10^{-6}/°C)
Bourdon tube	Stainless steel	8.0	194.76	−64.96	0.28	10.249 + 0.00299 T
Armature/Upper yoke/Lower yoke	Soft magnetic alloy	8.17	162.00	−23.20	0.3	9.27
Support tube/ Screw/Feedback rod	Elastomeric alloy	8.0	190.00	−26.00	0.3	13.0
Permanent magnet	Alnico magnet	7.15	150.00	−28.00	0.3	10.7
Adjusting shim	Stainless steel	7.8	198.13	−45.05	0.29	15.365 + 0.00584 T
Fixed base	Stainless steel	7.8	214.71	−32.74	0.29	9.772 + 0.00284 T
Support block	Aluminium alloy	2.85	72.15	−51.27	0.33	21.799 + 0.01043 T

Table A.2. Physical-mechanical parameters of each part for PMTM under T = 20∼200°C.

Parameters	Value(mm)	Parameters	Value(mm)
Length of the setscrews l_1	25.5	Length of mating segment of fixed base and setscrew l_7	3.65
Thickness of the horizontal segment of the upper yoke l_2	2.2	Length of the vertical segment of the upper yoke l_8	5.0
Length of the permanent magnet l_3	10.6	Length of the vertical segment of the lower yoke l_9	5.0
Thickness of the horizontal segment of the lower yoke l_4	2.2	Outer diameter of the bourdon tube D_{tube}	2.5
Thickness of the adjusting shim l_5	0.75	Inner diameter of the bourdon tube d_{tube}	2.5
Thickness of the support block l_6	4.1	Length of thin-wall section of the bourdon tube l_{tube}	7.2

$$\begin{aligned} T_{\mathrm{tm0}}\left(X_{g1},X_{g2},X_{g3},X_{g4},B_r\right)\big|_{B_r=0.58\mathrm{T}} =\ & 1.010\times10^{-4}-3.085\times10^{2}X_{g1}+3.875\times10^{2}X_{g2}-3.878\times10^{2}X_{g3}+3.083\times10^{2}X_{g4}\\ & -1.018\times10^{3}X_{g1}X_{g2}+1.103\times10^{3}X_{g1}X_{g3}+1.633\times10^{2}X_{g1}X_{g4}+4.754\times10^{2}X_{g2}X_{g3}\\ & -9.822\times10^{2}X_{g2}X_{g4}+1.237\times10^{3}X_{g3}X_{g4}+2.787\times10^{5}\left(X_{g1}\right)^2-3.348\times10^{5}\left(X_{g2}\right)^2\\ & +3.347\times10^{5}\left(X_{g3}\right)^2-2.789\times10^{5}\left(X_{g4}\right)^2 \end{aligned} \tag{A.1}$$

$$\begin{aligned} K_t\left(X_{g1},X_{g2},X_{g3},X_{g4},B_r\right)\big|_{B_r=0.58\mathrm{T}} =\ & 1.332-1.052\times10^{3}X_{g1}-9.356\times10^{2}X_{g2}-9.880\times10^{2}X_{g3}-1.022\times10^{3}X_{g4}\\ & +4.346\times10^{5}X_{g1}X_{g2}-4.794\times10^{5}X_{g1}X_{g3}+6.975\times10^{5}X_{g1}X_{g4}+1.061\times10^{5}X_{g2}X_{g3}\\ & -5.354\times10^{5}X_{g2}X_{g4}+4.388\times10^{5}X_{g3}X_{g4}+6.945\times10^{5}\left(X_{g1}\right)^2+4.061\times10^{5}\left(X_{g2}\right)^2\\ & +4.434\times10^{5}\left(X_{g3}\right)^2+6.799\times10^{5}\left(X_{g4}\right)^2 \end{aligned} \tag{A.2}$$

$$\begin{aligned} K_m\left(X_{g1},X_{g2},X_{g3},X_{g4},B_r\right)\big|_{B_r=0.58\mathrm{T}} =\ & 33.627-2.675\times10^{4}X_{g1}-3.011\times10^{4}X_{g2}-3.033\times10^{4}X_{g3}-2.663\times10^{4}X_{g4}\\ & +1.221\times10^{7}X_{g1}X_{g2}-1.051\times10^{7}X_{g1}X_{g3}+8.944\times10^{6}X_{g1}X_{g4}+1.983\times10^{7}X_{g2}X_{g3}\\ & -1.078\times10^{7}X_{g2}X_{g4}+1.221\times10^{7}X_{g3}X_{g4}+2.236\times10^{7}\left(X_{g1}\right)^2+1.966\times10^{7}\left(X_{g2}\right)^2\\ & +1.980\times10^{7}\left(X_{g3}\right)^2+2.233\times10^{7}\left(X_{g4}\right)^2 \end{aligned} \tag{A.3}$$

$$\begin{aligned} T_{\mathrm{tm0}}\left(X_{g1},X_{g2},X_{g3},X_{g4},B_r\right)\big|_{B_r=0.58\mathrm{T}} =\ & 0.85408\times10^{-4}-308.95X_{g1}+389.62X_{g2}-389.93X_{g3}+308.81X_{g4}\\ & -1609.7X_{g1}X_{g2}+4639.5X_{g1}X_{g3}+16.401X_{g1}X_{g4}+121.15X_{g2}X_{g3}\\ & -4648.6X_{g2}X_{g4}+1955.5X_{g3}X_{g4}+278390\times\left(X_{g1}\right)^2-335580\times\left(X_{g2}\right)^2\\ & +335720\times\left(X_{g3}\right)^2-278410\times\left(X_{g4}\right)^2(Forthird-orderresponsesurface) \end{aligned} \tag{A.4}$$

$$\begin{aligned} K_t\left(X_{g1},X_{g2},X_{g3},X_{g4},B_r\right)\big|_{B_r=0.58\mathrm{T}} =\ & 1.3636-1087.3X_{g1}-975.11X_{g2}-1041X_{g3}-1051.1X_{g4}\\ & +612870X_{g1}X_{g2}-610760X_{g1}X_{g3}+842680X_{g1}X_{g4}+1280300X_{g2}X_{g3}\\ & -686000X_{g2}X_{g4}+618640X_{g3}X_{g4}+642140\times\left(X_{g1}\right)^2+333070\times\left(X_{g2}\right)^2\\ & +379020\times\left(X_{g3}\right)^2+625950\times\left(X_{g4}\right)^2(Forthird-orderresponsesurface) \end{aligned} \tag{A.5}$$

$$\begin{aligned} K_m\left(X_{g1},X_{g2},X_{g3},X_{g4},B_r\right)\big|_{B_r=0.58\mathrm{T}} =\ & 33.809-27083X_{g1}-30205X_{g2}-30774X_{g3}-26767X_{g4}\\ & +12109000X_{g1}X_{g2}-9950000X_{g1}X_{g3}+8866300X_{g1}X_{g4}+19947000X_{g2}X_{g3}\\ & -10603000X_{g2}X_{g4}+12150000X_{g3}X_{g4}+22626000\times\left(X_{g1}\right)^2+19696000\times\left(X_{g2}\right)^2\\ & +20095000\times\left(X_{g3}\right)^2+22485000\times\left(X_{g4}\right)^2(Forthird-orderresponsesurface) \end{aligned} \tag{A.6}$$